remote sensing

Article

Salinity Fronts in the South Atlantic

Igor M. Belkin * and Xin-Tang Shen

College of Marine Science and Technology, Zhejiang Ocean University, Zhoushan 316022, China; shenxintang@zjou.edu.cn
* Correspondence: igormbelkin@gmail.com

Abstract: Monthly climatology data for salinity fronts in the South Atlantic have been created from satellite SMOS sea surface salinity (SSS) measurements taken from 2011–2019, processed at the Barcelona Expert Center of Remote Sensing (BEC), and provided as high-resolution (1/20°) daily SSS data. The SSS fronts have been identified with narrow zones of enhanced horizontal gradient magnitude (GM) of SSS, computed using the Belkin–O'Reilly algorithm (BOA). The SSS gradient fields generated by the BOA have been log-transformed to facilitate feature recognition. The log-transformation of SSS gradients markedly improved the visual contrast of gradient maps, which in turn allowed new features to be revealed and previously known features to be documented with a monthly temporal resolution and a mesoscale (~100 km) spatial resolution. Monthly climatologies were generated and analyzed for large-scale open-ocean SSS fronts and for low-salinity regions maintained by the Rio de la Plata discharge, Magellan Strait outflow, Congo River discharge, and Benguela Upwelling. A 2000 km-long triangular area between Africa and Brazil was found to be filled with regular quasi-meridional mesoscale striations that form a giant ripple field with a 100 km wave length. South of the Tropical Front, within the subtropical high-salinity pool, a trans-ocean quasi-zonal narrow linear belt of meridional SSS maximum (Smax) was documented. The meridional Smax belt shifts north–south seasonally while retaining its well-defined linear morphology, which is suggestive of a yet unidentified mechanism that maintains this feature. The Subtropical Frontal Zone (STFZ) consists of two tenuously connected fronts, western and eastern. The Brazil Current Front (BCF) extends SE between 40 and 45°S to join the subantarctic front (SAF). The STFZ trends NW–SE across the South Atlantic, seemingly merging with the SAF/BCF south of Africa to form a single front between 40 and 45°S. In the SW Atlantic, the Rio de la Plata plume migrates seasonally, expanding northward in winter (June–July) from 39°S into the South Brazilian Bight, up to Cabo Frio (23°S) and beyond. The inner Plata front moves in and out seasonally. Farther south, the Magellan Strait outflow expands northward in winter (June–July) from 53°S up to 39–40°S to nearly join the Plata outflow. In the SE Atlantic, the Congo River plume spreads radially from the river mouth, with the spreading direction varying seasonally. The plume is often bordered from the south by a quasi-zonal front along 6°S. The diluted Congo River water spreads southward seasonally down to the Angola–Benguela Front at 16°S. The Benguela Upwelling is delineated by a meridional front, which extends north alongshore up to 20°S, where the low-salinity Benguela Upwelling water forms a salinity front, which is separate from the thermal Angola–Benguela Front at 16°S. The high-salinity tropical water ("Angola water") forms a wedge between the low-salinity waters of the Congo River outflow and Benguela Upwelling. This high-salinity wedge is bordered by salinity fronts that migrate north–south seasonally.

Keywords: ocean front; salinity; South Atlantic; SMOS

check for updates

Citation: Belkin, I.M.; Shen, X.-T. Salinity Fronts in the South Atlantic. *Remote Sens.* **2024**, *16*, 1578. https://doi.org/10.3390/rs16091578

Academic Editor: Ebenezer Sackitey Nyadjro

Received: 17 March 2024
Revised: 22 April 2024
Accepted: 25 April 2024
Published: 29 April 2024

1. Introduction

Sea water salinity is an important oceanic variable that plays a key role in numerous physical and biogeochemical processes. Salinity fronts—narrow zones where fresh and salty waters meet—play special roles, especially in tropical and subtropical regions. Along salinity fronts in the subtropics, warm and salty subtropical waters meet colder, fresher subpolar waters of similar density; thus, these fronts are partly or completely density compensated. In the tropics, copious rains and freshwater discharges from great rivers produce surface water masses of low density; therefore, salinity fronts in the tropics often feature strong density gradients. In both cases (tropics and subtropics), salinity fronts shape ocean circulation by either enhancing (in the tropics) or reducing (in the subtropics) horizontal density gradients created by temperature gradients (Boutin et al., 2023) [1]. Salinity fronts mark water mass boundaries in the tropics, where surface water masses may have similar temperatures, yet different salinities. Typically, thermal and haline manifestations of the same fronts are collocated. However, sometimes thermal and haline signatures diverge, which further illustrates the importance of studying salinity fronts and their associations with temperature fronts in the World Ocean.

Remote sensing of salinity fronts on a global scale began in this century, owing to three satellite missions—SMOS, Aquarius, and SMAP—that carried radiometers whose data were used to estimate sea surface salinity (SSS; Reul et al., 2014 [2]; Boutin et al., 2018 [3]; Vinogradova et al., 2019 [4]; Reul et al., 2020 [5]; Boutin et al., 2021 [6]; Boutin et al., 2023 [1]). The SSS data from all three missions have been used, albeit sporadically, to study space-time variability of *salinity fronts*, mostly in the tropics (Qu et al., 2014 [7]; Kao and Lagerloef, 2015 [8]; Yu, 2015 [9]; Melnichenko et al., 2016 [10]; Nyadjro and Subrahmanyam, 2016 [11]; Asto et al., 2019 [12]; Reul et al., 2020 [5]; Bao et al., 2021 [13]; Boutin et al., 2023 [1]; Vazquez-Cuervo et al., 2023 [14]). Yet, despite the proven potential of satellite SSS data, the global climatology of salinity fronts is lacking. The potential importance of such climatology was the main impetus for this study. We choose to focus first on the fronts of the Southern Hemisphere, because they are less studied compared with the fronts of the Northern Hemisphere. The present report on the South Atlantic will be followed by similar reports on the South Indian and South Pacific oceans. The structure of this paper is as follows: Section 1 introduces numerous South Atlantic fronts and remote sensing studies of these fronts, thereby providing a background for our study. Satellite SSS data and data processing are described in Section 2. Results are presented in Section 3, followed by the Discussion in Section 4, and Conclusions in Section 5.

Remote sensing of ocean fronts in the South Atlantic: The seminal survey of sea surface temperature (SST) fronts by Legeckis (1978) [15] ushered in an era of remote sensing studies of ocean fronts. Table 1 provides a provisional inventory of remote sensing studies of the South Atlantic, followed by a brief regional introduction to the most important studies of fronts and frontal zones of this vast region, between the equator and Antarctic Circumpolar Current (ACC). Table 1 includes studies based on four major oceanic observables—SST, SSS, SSH, and CHL—because a combined use of different observables is helpful in detecting fronts. Throughout our paper, we have cited numerous frontal studies listed in Table 1, which provides the most important metadata about these studies.

Brazil Current/Front/Retroflection and Brazil-Malvinas Confluence: Among the most conspicuous thermal fronts in the World Ocean surveyed with early infrared satellite imagery, Legeckis (1978) [15] emphasized the Brazil-Malvinas Confluence, a major water mass front between subtropical and subantarctic waters. Legeckis and Gordon (1982) [37] reported intra-seasonal north–south migrations of the Brazil Current/Front. The advent of AVHRR in 1981 and subsequent implementation of the Pathfinder project (Minnett et al., 2019) [57] stimulated studies of SST fronts, particularly in those areas where various physical processes create enhanced thermal contrasts between adjacent water masses. Such areas are mostly found in the coastal regions of the SW Atlantic and Eastern Atlantic. In the SW Atlantic, the Brazil Current/Front/Retroflection and Brazil-Malvinas Confluence have been studied by Olson et al. (1988) [47], Provost et al. (1996) [58], Saraceno et al. (2004) [52], Barré et al. (2006) [18], Lorenzzetti et al. (2009) [38], Artana et al. (2018) [17], Artana et al. (2019) [59], Castellanos et al. (2019) [22], and da Silveira et al. (2023) [25].

Table 1. Satellite studies of the South Atlantic.

Reference	Variable	Period	Sensor/Mission	Region
Allega et al., 2021 [16]	SST	1985–2019	AVHRR, MODIS	Patagonian Shelf
Artana et al., 2018 [17]	SST, SSH	2007–2016	Multisensor; Altimeters	SW Atlantic
Barre et al., 2006 [18]	SST, color	2002–2004	MODIS, SeaWiFS	Brazil-Malvinas Confluence
Belkin & Shen 2024 (this study)	SSS	2011–2019	SMOS	South Atlantic (0–60°S)
Billany et al., 2010 [19]	SSH	1993–2007	Altimeters	Greenwich Meridian
Bouali et al., 2017 [20]	SST	2003–2014	MODIS	South Atlantic (0–60°S)
Burls & Reason 2006 [21]	SST	2002–2005	TRMM, AMSR-E	South Atlantic (25–55°S)
Castellanos et al., 2019 [22]	SSS	2011–2015	SMOS	SW Atlantic; SE Atlantic; 12mos
Chao et al., 2015 [23]	SSS	2011–2013	Aquarius	Congo River plume
Chen et al., 2019 [24]	SST	2002–2016	MODIS	SE Brazil; Shelf fronts
Da Silveira et al., 2023 [25]	SST SSH	2002–2020 1993–2020	Multi-sensor Altimeters	Brazil Current, 22–23°S
Dencausse et al., 2011 [26]	SSH	1992–2007	Altimeters	SE Atlantic (5°W–35°E)
Dong et al., 2006 [27]	SST	2002–2005	AMSR-E	Polar Front
Franco et al., 2008 [28]	SST	1985–2002	AVHRR	Patagonian Shelf; SBF (39–44°S)
Franco et al., 2022 [29]	SST SSH CHL	1993–2019 1993–2019 2002–2020	Multi-sensor Altimeters MODIS	Patagonian Shelf
Freeman & Lovenduski 2016 [30]	SST	2002–2014	Microwave radiometers	Polar Front
Graham & de Boer 2013 [31]	SST SSH	1999–2009 1999–2009	AVHRR Altimeters	Subtropical Front
Guerrero et al., 2014 [32]	SSS	2010–2013 2011–2013	SMOS Aquarius	SW Atlantic
Hopkins et al., 2013 [33]	SST SSS CHL SSH	2010	AVHRR, AMSR SMOS MODIS, MERIS Altimeters	Congo River plume
Hösen et al., 2016 [34]	SST	2006–2011 2011–2014	AMSR-E/MODIS 9 km MODIS 4 km	Benguela Upwelling filaments
Houndegnonto et al., 2021 [35]	SSS	2010–2017	SMOS	Congo River plume
Kim & Orsi 2014 [36]	SSH	1992–2011	Altimeters	ACC fronts
Legeckis & Gordon 1982 [37]	SST	1975–1978	VHRR	Brazil-Malvinas Confluence
Lorenzzetti et al., 2009 [38]	SST	2000–2002	AVHRR	Brazil Current
Luko et al., 2021 [39]	Velocity	1993–2018	Altimeters	South Equatorial Current
Lutjeharms & Meeuwis 1987 [40]	SST	1982–1985	AVHRR	SE Atlantic; Benguela Upwelling
Lutjeharms et al., 1993 [41]	SST	1988	AVHRR	Subtropical Front
Martins & Stammer 2022 [42]	SSS	2010–2020	SMOS, Aquarius, SMAP	Congo River plume
Meeuwis & Lutjeharms 1990 [43]	SST	1982–1985	AVHRR	Angola-Benguela Current
Melnichenko et al., 2016 [10]	SSS	2011–2015	Aquarius	Global
Meeuwis 1991 [44]	SST	1982–1985	AVHRR	South Atlantic and South Indian
Moore et al., 1997 [45]	SST	1987–1988	AVHRR	Polar Front, 90°W–20°W
Moore et al., 1999 [46]	SST	1987–1993	AVHRR	Polar Front, Circumpolar
Olson et al., 1988 [47]	SST	1981–1987	AVHRR	Brazil-Malvinas Confluence
Piola et al., 2008a [48]	CHL	1998–2005	SeaWiFS	Rio de la Plata plume

Table 1. *Cont.*

Reference	Variable	Period	Sensor/Mission	Region
Reul et al., 2014 [2]	SSS	2010–2012	SMOS	Congo River plume
Rivas 2010 [49]	SST	1985–2002	AVHRR	Southwest Atlantic
Rivas & Pisoni 2010 [50]	SST	1985–2002	AVHRR	Patagonian Shelf
Ruiz-Etcheverry & Saraceno 2020 [51]	SSH	1993–2017	Altimeters	South Atlantic (36–55°S)
Saraceno et al., 2004 [52]	SST	1987–1995	AVHRR	Brazil-Malvinas Confluence
Saraceno et al., 2005 [53]	SST CHL	1998–2003 1998–2003	AVHRR, AMSR-E SeaWiFS	Southwest Atlantic
Veitch et al., 2006 [54]	SST	1982–1999	AVHRR	Angola-Benguela Front
Wang et al., 2021 [55]	SST CHL	2004–2019 2007–2019	Multi-sensor MODIS	SW Atlantic
Wang et al., 2023 [56]	SST SSH	2010–2018 2010–2018	AVHRR Altimeters	SW Atlantic
Yu et al., 2015 [9]	SSS	2012–2013	Aquarius	Tropical Atlantic

The Rio de la Plata plume features prominently in the salinity field. The Plata discharges over 22,000 m^3/s on average, and up to 60,000 m^3/s at maximum (Guerrero et al., 1997 [60]; Piola et al., 2005 [61]; Acha et al., 2008 [62]; Campos et al., 2008 [63]). The Plata discharge is made of two major components, Paraná and Uruguay, that are anticorrelated; therefore, the seasonal variations of Plata discharge are relatively small, varying between 20,000 and 27,000 m^3/s according to Figure 8 in Dogliotti et al. (2016) [64], based on discharge data by Borús and Giacosa (2014) [65]. The first-ever synoptic aerial survey of the Plata Plume in winter 2003 documented the Plume's northward extent of 1100 km up to Itajaí (Brazil) at 27°S (Burrage et al., 2008) [66]. According to the modeling study by Piola et al. (2005) [61], the Plata Plume extends north for up to 1300 km. In winter 1993, following an anomalously high Plata discharge, Plata water extended north by 1500 km up to 23°S (Campos et al., 1996 [67]; Campos et al., 1999 [68]; Campos et al., 2008 [63]). Analysis of historical precedents by Campos et al. (1999) [68] showed that the penetration of Plata water into the South Brazil Bight is not an unusual event. The Plata water's northward penetration is driven largely by wind stress rather than variations in the Plata discharge (Palma et al., 2008) [69].

The Plata plume and associated fronts were studied, among others, by Guerrero et al. (1997) [60], Garcia and Vargas (1998) [70], Framiñan et al. (1999) [71], Simionato et al. (2001) [72], Möller et al. (2008) [73], Moreira and Simionato (2019) [74], and Lisboa et al. (2022) [75], and were recently reviewed by Piola et al. (2018) [76]. The Plata Plume front is prominent in salinity, and it also manifests in SST in summer, when the Plata outflow is warmer than offshore waters (Figure 6 in uerreroetal.,1997 [60]; Figure 8.13 in ramiñanetal., 1999 [71]). The collocated turbidity front was studied, among others, by Framiñan and Brown (1996) [77], Dogliotti et al. (2016) [64], and Maciel et al. (2021) [78]. The salinity front was studied, based on SMOS and Aquarius SSS data, by Guerrero et al. (2014) [32].

The Patos Lagoon outflow, with average discharge of 2000 m^3/s (~10% of the Plata discharge), creates a plume that extends up to >30 km offshore across the inner shelf and >100 km alongshore, and is bordered by a sharp salinity front with a cross-frontal step of 10 psu. It is embedded in the Plata plume (Burrage et al., 2008) [66]. The impact of both plumes on salinity variability and cross-shelf exchanges was studied by Matano et al. (2014) [79].

The Patagonian Shelf features fronts of various nature (Acha et al., 2004 [80]; Rivas and Pisoni, 2010 [50]; Piola et al., 2018 [76]; Brun et al., 2020 [81]), including tidal mixing fronts (Glorioso, 1987) [82], especially in the Gulf of San Jorge (Palma et al., 2020) [83] and off Península Valdés. The Patagonian Shelf is bordered by the **Shelf-Break Front** (Franco et al., 2008 [28]; Combes and Matano, 2018 [84]; Franco et al., 2022 [29]).

The Subtropical Shelf Front was identified first from in situ data by Piola et al. (2000) [85], who also studied this front based on satellite data (Piola et al., 2008b) [86]. Cross-shelf oceanographic sections by Muelbert et al. (2008) [87] revealed a strong two-step ("double") thermohaline front in winter (T = 12–18 °C, S = 33.0–36.5), when this TS-front extended vertically from the sea surface to the shelf break, whereas in summer this front manifested in salinity only (S = 33.7–35.2).

Surface thermal fronts of the SW Atlantic were studied from satellite SST data by Saraceno et al. (2005) [53], Rivas (2010) [49], Rivas and Pisoni (2010) [50], Bouali et al. (2017) [20], Wang et al. (2021) [55], and Wang et al. (2023) [56].

Magellan Plume: The surface salinity field of the southern Patagonian Shelf is strongly affected by the inflow of low salinity water from the Magellan Strait, Le Maire Strait, and along the Cape Horn shelf break (Palma and Matano, 2012 [88]; Brun et al., 2020 [81]; Guihou et al., 2020 [89]). Brun et al. (2020) [81] presented an up-to-date climatological map of salinity at 20 m depth over the Patagonian Shelf from in situ data (Figure 2 in [81]). This map shows the freshwater outflow from the Magellan Strait extending north up to 43°S. This flow transports up to 0.074 Sv, thereby providing "a strong interoceanic connectivity associated with diluted subantarctic waters of the Pacific Ocean through the Magellan Strait which in turn are further diluted largely by inflows from the Almirantazgo Fjord via the Whiteside Channel. ... The low salinity inflow from the Magellan Strait combines with saltier inflows through the Le Maire Strait and farther east that feed the Atlantic shelf". (*ibid.*, p. 1).

The Congo River outflow, with long-term (2000–2010) annual mean discharge of 40,662 m^3/s (Alsdorf et al., 2016) [90], creates a huge freshwater plume whose space-time variability and dynamics have been extensively studied (Denamiel et al., 2013 [91]; Hopkins et al., 2013 [33]; Reul et al., 2014 [2]; Vic et al., 2014 [92]; Chao et al., 2015 [93]; Sorí et al., 2017 [94]; Munzimi et al., 2019 [95]; Phillipson and Toumi, 2019 [96]; Laraque et al., 2020 [97]; Houndegnonto et al., 2021 [35]; Martins and Stammer, 2022 [42]; Jarugula and McPhaden, 2023 [98]; Wongchuig et al., 2023 [99]). Similar to other river plumes, the Congo River plume could feature *fronts* in SST and SSS that could either bound the plume, or be embedded in the plume; however, this aspect of the Congo River outflow remained unexplored to date. Chao et al. (2015) [23] studied offshore freshwater anomalies created by variations in the Congo River outflow in 2011–2013. When the Congo River discharge quadrupled between August 2012 and January 2013, this caused an offshore low-salinity anomaly (observed along Aquarius orbital tracks some 400 km from the river mouth) that peaked in February 2013, about a month after the discharge peak of >60,000 m^3/s in January 2013 (Figures 5 and 9 in [23]) (see also [93] for more data and analyses of the Congo River hydrology).

The main water mass front In the Eastern Atlantic is **the Angola–Benguela Front (ABF)** at the confluence of the warm southward Angola Current and the cold northward Benguela Current (Shannon et al., 1987 [100]; Meeuwis and Lutjeharms, 1990 [43]; Lass et al., 2000 [101]; Mohrholz et al., 2004 [102]; Veitch et al., 2006 [54]; Vizy et al., 2018 [103]). This quasi-zonal front migrates in the general north–south direction seasonally, spanning a wide range of latitudes and including multiple fronts, thus called the Angola–Benguela Frontal Zone.

Another prominent frontal zone in the SE Atlantic is associated with the **Benguela Upwelling** (Andrews and Hutchings, 1980 [104]; Lutjeharms and Meeuwis, 1987 [40]; Hutchings et al., 2009 [105]). The upwelling gives rise to upwelling fronts, particularly in the southern Benguela, between Cape Agulhas (35°S) and Cape Columbine (33°S) (Hutchings et al., 1986 [106]; Armstrong et al., 1987 [107]). The **Benguela Upwelling Frontal Zone** (Belkin et al., 2009) [108] consists of two isolated frontal zones separated at the Lüderitz line (27°S). This separation has been documented by Duncombe Rae (2005) [109] and is collocated with the area of high winds and low chlorophyll at 26–27°S, as pointed out by Hutchings et al. (2009) [105]. This separation is also nearly collocated with a sharp bathymetric change at about 28°S, where the broad shelf to the south contrasts with the narrow shelf to the north. In addition to a strong negative signal in SST, the Benguela Upwelling manifests as a negative signal in SSS (up to −0.6 psu), which has been documented, among others, by Muller et al. (2013) [110] and Hösen et al. (2016) [34], with the latter providing statistics on 450 upwelling filaments that extend up to >500 km offshore.

Compared to coastal fronts, **open-ocean fronts** have attracted less attention. Belkin (1993) analyzed sparse historical data to distinguish the North and South STF some 400–500 km apart, thus forming the **Subtropical Frontal Zone (STFZ)**, extending quasi-zonally at 35–40°S. This double-front pattern was confirmed, among others, by Belkin and Gordon (1996) [111] and Smythe-Wright et al. (1998) [112], and is consistent with the double-front pattern of STF presented by Lutjeharms et al. (1993) [41]. In the central South Atlantic, Juliano and Alves (2007) [113] documented a major zonal current/front at 34–35°S and termed it the **St. Helena Current/Front** after the St. Helena high pressure system centered over St. Helena Island at 20°S. Vianna and Menezes (2011) [114] noted this geographic incongruence and termed this jet the **Tristan da Cunha Current** after the Tristan da Cunha Islands at 37°S. Burls and Reason (2006) [21] studied SST fronts between 25°S and 55°S. Funke (2009) [115] used satellite data to study the STF in the central South Atlantic. Billany et al. (2010) [19] studied fronts at the Greenwich Meridian. Dencausse et al. (2011) [26] studied the STFZ in the SE Atlantic. Bouali et al. (2017) [20] estimated 12-year trends of SST gradients (fronts) across the entire South Atlantic. The **Subantarctic Front (SAF)** observed at 45–50°S in numerous in situ studies has never been comprehensively studied from satellite data (save for the Meeuwis (1991) [41] PhD study) as opposed to the **Polar Front (PF)**, which has been a subject of several remote sensing studies. In this regard, Peterson and Stramma (1991, p. 47) [116] noted: "The course of the SAF has been studied to a much lesser extent than that of the PF, which is partly because the SAF is not always clear in the surface temperature fields; it is better identified with upper-layer salinities". The Polar Front has been mapped by Moore et al. (1997) [45], Moore et al. (1999) [46], Dong et al. (2006) [27], and Freeman and Lovenduski (2016) [30].

2. Data and Methods

SSS Data: We used SSS data from SMOS (Kerr et al., 2010 [117]; Reul et al., 2014 [2]; Boutin et al., 2018 [3]; Reul et al., 2020 [5]; Boutin et al., 2021 [6]; Boutin et al., 2023 [1]). We used *high-resolution* SMOS SSS data provided by the Barcelona Expert Center (BEC; smos-bec@icm.csic.es), in which nine years (2011–2019) of SMOS data were reprocessed and daily global SSS maps generated, as documented by Olmedo et al. (2021) [118]. We used BEC Level 4 SMOS SSS daily data with a horizontal resolution of 0.05° × 0.05°, or approximately 5.6 km × 5.6 km at the equator. These data were downloaded from https://bec.icm.csic.es/bec-ftp-service/ (accessed 24 April 2024).

Front detection: We used the Belkin and O'Reilly (2009) [119] algorithm (BOA) to calculate horizontal gradients of SSS. High-gradient zones were identified with salinity fronts. The BOA is widely used thanks to its efficiency and simplicity (Belkin, 2021) [120]. The BOA uses a contextual shape-preserving, scale-sensitive, adaptive median filter that effectively eliminates impulse/shotgun/salt-and-pepper noise. At the same time, the BOA does not smooth ramp-like steps (fronts). It also retains intact roof-like ridges and significant peaks or valley-like minima (local pointwise freshening events). The BOA's median filter can be applied iteratively. The iterative median filter, when applied to a one-dimensional dataset (e.g., a time series), is known to converge to a root signal (Gallagher and Wise, 1981) [121]. However, when applied to a 2D dataset (e.g., an image), the iterative median filter does not necessarily converge. Our experiments with the BOA's iterative MF confirmed the lack of convergence while processing daily mean global SMOS SSS fields. The main reason for that is probably the overall smoothness of BEC L4 data. Therefore, after the first 10–20 iterations, when the MF removes remaining noise, the subsequent iterations do not result in any improvement. Therefore, the number of iterations can be kept to a minimum.

Logarithmic transformation of data: Logarithmic transformation (or log-transform) of experimental and remote sensing data has a long history (Irons and Petersen, 1981 [122]; Currant-Everett, 2018 [123]). A typical situation in which log-transform is needed is when the distribution of experimental data are highly skewed. When data distributions are far from normal, statistical tests developed for normally distributed data cannot be applied. Also, highly skewed 2D data are difficult to visualize, especially when the data range spans a few orders of magnitude, which is a common situation in digital image processing (Gonzalez and Woods, 2018 [124]; Gonzalez et al., 2020 [125]), including digital processing of satellite imagery.

Log-transform in satellite oceanography: In oceanography, following the seminal work by Campbell (1995) [126], the log-transform method has been routinely applied to CHL data, particularly to global CHL data provided by satellites, because (1) the global distribution of original CHL data is highly skewed, and (2) the global CHL data range is wide (Gregg and Casey, 2004 [127]; Werdell et al., 2018 [128]). Other oceanic remotely sensed observables are almost never transformed, since the observed data do not span orders of magnitude, especially in the open ocean, and also because their distributions are not highly skewed. The above does not apply to some derived quantities, e.g., gradients. For example, Zhang et al. (2014) [129] have log-transformed the gradient magnitude (GM) of SST data from the Taiwan Strait and demonstrated the lognormality of GM data.

Log-transform of SSS gradient: To bring out SSS fronts, we ran the BOA algorithm (Belkin and O'Reilly, 2009) [119] over SSS data to obtain salinity gradients. Maps of the gradient magnitude (GM) of SSS revealed zones of enhanced GM, which represented salinity fronts. The frequency distribution of GM was strongly skewed; therefore, we log-transformed GM using natural logarithms (ln). The frequency distribution of the log-transformed gradient ln(GM(SSS)) was symmetrical and fairly normal, while the maps of log-transformed gradient presented in the next section reveal more features, particularly fronts. Using the terminology of digital image processing, the log-transform enhances contrasts across digital maps (Gonzalez and Woods, 2018 [124]; Gonzalez et al., 2020 [125]). Experiments have shown that log-transformation of original SSS data slightly improves the visual contrast of gradient maps, although this additional preprocessing step is not critical, while log-transformation of the gradient is crucial.

3. Results

3.1. Large-Scale Open-Ocean Salinity Fronts

3.1.1. Large-Scale Pattern of Sea Surface Salinity

The large-scale (ocean-wide) pattern of SSS is fairly stable year-round, as evidenced by long-term (2011–2019) mean monthly maps of SSS that feature a low-salinity equatorial belt, high-salinity subtropical pool, and general salinity decrease due south toward 45–50°S (Figure 1a (January–June) and Figure 1b (July–December)).

Superimposed on this ocean-scale pattern, there are four large-to-mesoscale regions of low-salinity: (1) Rio de Plata region; (2) Magellan Strait region; (3) Congo River region; and (4) Benguela Upwelling region. The ocean-wide maps of SSS do not reveal visually apparent zones of high horizontal gradients of SSS (salinity fronts), except for salinity fronts that border the outflows of two great rivers, Rio de la Plata and Congo. The large-scale open-ocean pattern of SSS does not qualitatively change seasonally. Unlike the large-scale open-ocean fronts that remain fairly stable seasonally, the above-mentioned four large-to-mesoscale regions off the coasts of South America and Africa experience substantial seasonal variability, as reported below.

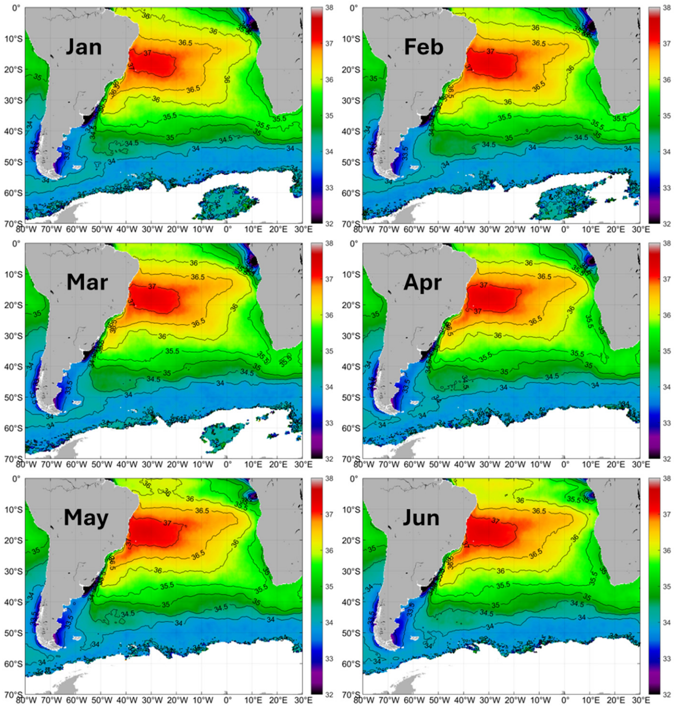

(**a**)

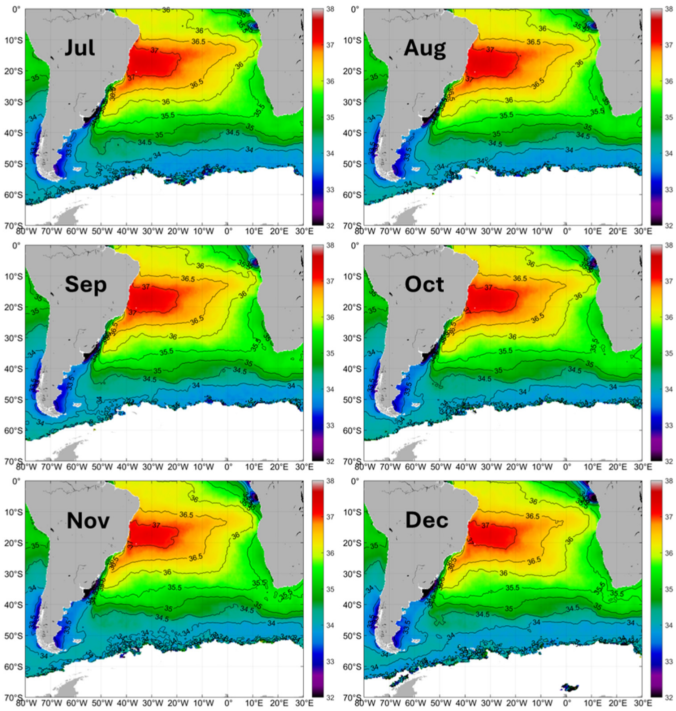

(**b**)

Figure 1. (**a**) Long-term (2011–2019) mean monthly maps of SSS, January–June. (**b**) Long-term (2011–2019) mean monthly maps of SSS, July–December.

3.1.2. Salinity Fronts: An Overview

Salinity fronts are visualized by (1) running the BOA algorithm that calculates gradients of SSS after filtering out impulse noise while preserving fronts, and (2) log-transforming SSS gradient magnitude (GM) (Figure 2a,b) The following large-scale open-ocean quasi-zonal fronts can be distinguished in all monthly maps, north to south: (1) Tropical Front (TF) between 10 and 15°S; (2) Western Subtropical Front (WSTF) near 30°S; (3) Eastern Subtropical Front (ESTF) near 35–40°S; (4) Brazil Current Front (BCF) between 40 and 45°S,

(5) Subantarctic Front (SAF) near 45°S, and (6) joint STF/BCF/SAF front south of Africa near 45°S. In addition to these high-gradient zones (fronts), we detected a quasi-zonal narrow belt of near-zero gradient that crosses the Tropical Atlantic south of the Tropical Front, between 15 and 20°S.

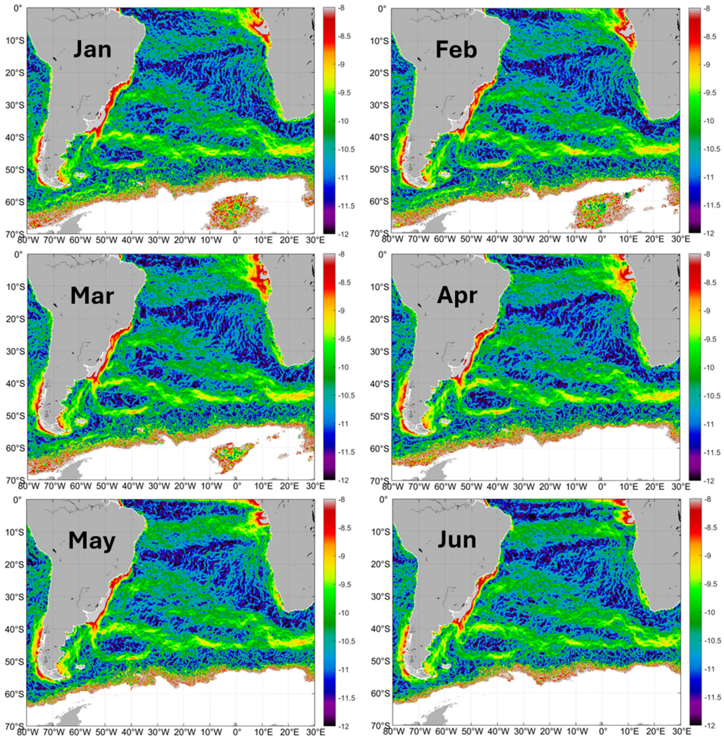

(**a**)

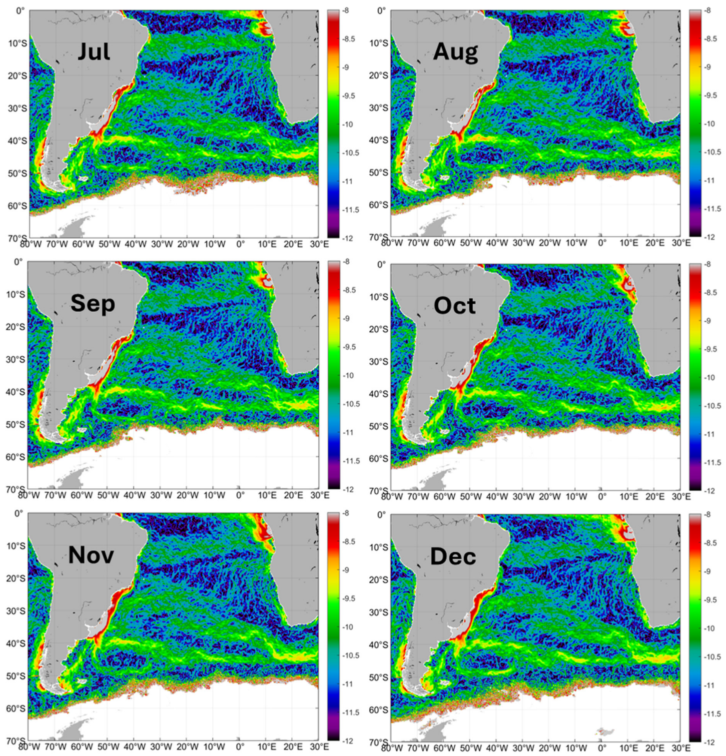

(**b**)

Figure 2. (**a**) Log-transformed gradient magnitude GM of sea surface salinity SSS, January–June. (**b**) Log-transformed gradient magnitude GM of sea surface salinity SSS, July–December.

3.1.3. Meridional (North-South) and Zonal (West-East) Variations of Surface Salinity

We used cross-frontal distributions of SSS to study along-front variability of frontal parameters, first of all to study along-front variations of cross-frontal ranges ("steps") of SSS. This is the most effective and efficient approach for mapping large-scale fronts across ocean-scale distances. This approach is based on assembling a set of cross-frontal sections arranged along the front in question, extracting frontal parameters (e.g., cross-frontal steps of T and S) along each section, and analyzing the along-front variability of these parameters. This approach has been used in numerous frontal studies, e.g., Stramma and Peterson (1990) [130], Belkin (1993) [131], and Belkin and Gordon (1996) [111], to name just a few.

Since the above-mentioned large-scale fronts are quasi-zonal, their main characteristics (intensity and strength) are best determined along meridians that cross the fronts quasi-normally. We chose 14 meridians spaced 5° of longitude apart, from 45°W to 20°E. Distributions of SSS vs. latitude along every 10° of longitude are shown in Figure 3.

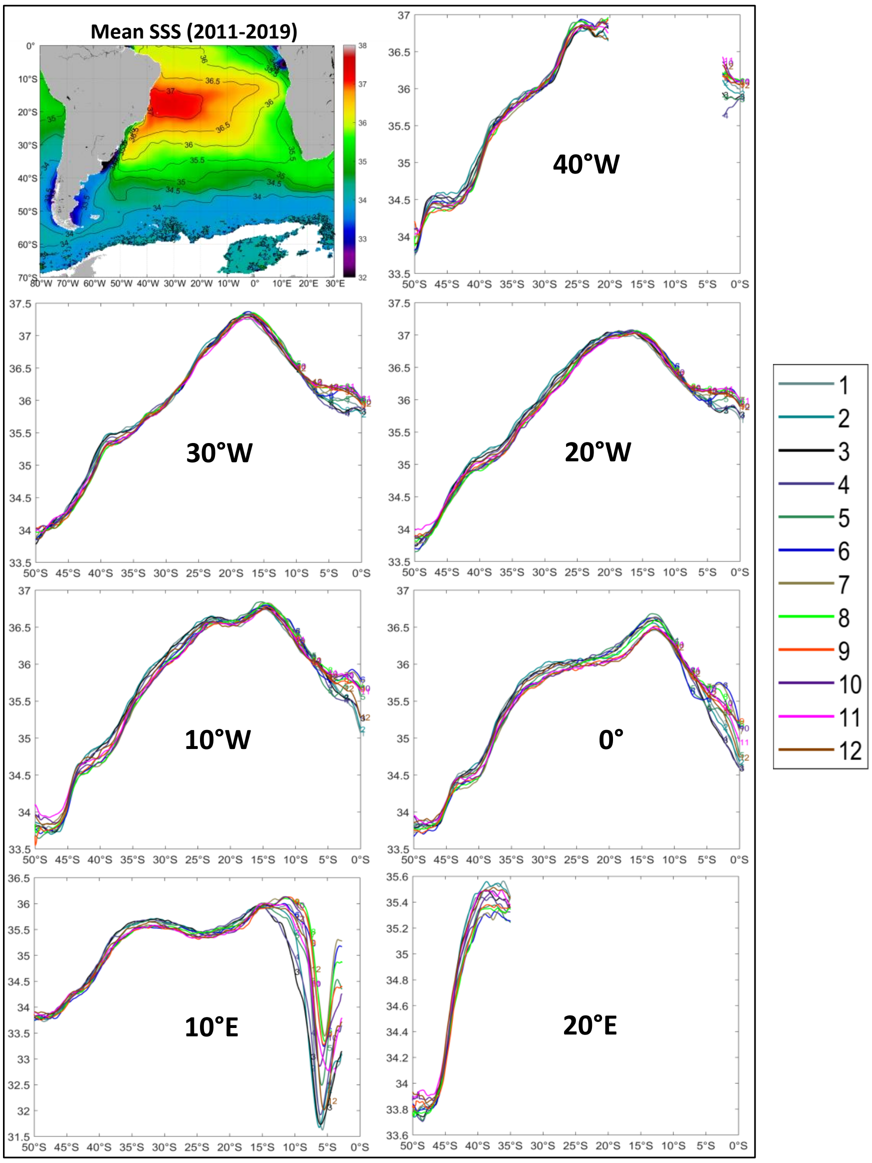

Figure 3. Long-term (2011–2019) mean monthly distributions of SSS along 7 meridians between 40°W and 20°E from the equator to 50°S. Monthly curves are numbered as in the legend (1 January, ... 12 December).

Each subplot shows 12 long-term (2011–2019) mean monthly distributions of SSS vs. latitude along a given meridian, illustrating the year-round stability of the meridional (north–south) pattern of SSS, except for the equatorial belt and Congo River outflow. Similar meridional distributions of SSS vs. latitude for individual years, 2011 through 2019 (not shown), document the interannual stability of the meridional (north–south) pattern of SSS, except for the equatorial belt and Congo River outflow. The seasonal and interannual stability of the meridional (north–south) distributions of SSS contrasts sharply with the relatively strong zonal (west–east) variations in the meridional distributions of SSS. Indeed, substantial qualitative (morphological) changes in the meridional distributions of SSS occur between meridians just 5° of longitude apart (that is, <500 km at 30°S). Thus, the large-scale meridional pattern of SSS experiences qualitative changes in the west–east direction at the upper mesoscale (500 km).

3.1.4. Large-Scale Pattern of Open-Ocean Salinity Fronts

The large-scale open-ocean salinity fronts appear as broad zones of enhanced gradient that are several hundred kilometers wide (Figures 1–3). The apparent breadth of salinity fronts can be partly accounted for by the original spatial resolution of SMOS data (35–50 km). It cannot be accounted for by temporal averaging of daily SMOS data used in this study, as evidenced by sample comparisons of daily, monthly, annual, and multi-annual (2011–2019) mean meridional (north-south) distributions of SSS. Owing to the temporal stability of large-scale open-ocean salinity fronts, these fronts retain their main characteristics, such as width and gradient, after temporal averaging on monthly, annual, and multi-annual scales. The rather smooth large-scale appearance of meridional distributions of SSS is not unusual, as it has been observed elsewhere, e.g., in the North Atlantic (Kolodziejczyk et al., 2015) [132].

3.1.5. Tropical Front

A close inspection of monthly gradient maps (Figure 2) reveals (1) seasonal migrations of the Tropical Front in the north–south direction, and (2) seasonal variations in the spatial orientation of this front. The north–south range of seasonal migration is rather small (about 2° of latitude). The front's spatial orientation ("tilt") varies seasonally in sync with the front's north–south seasonal migrations. When the front reaches its northernmost location, its orientation is strictly zonal. When the front reaches its southernmost location, its non-zonal orientation (tilt) is at maximum.

3.1.6. Meridional Salinity Maximum

Immediately south of the Tropical Front, a narrow quasi-zonal band of zero salinity gradient, which corresponds to the meridional salinity maximum (Smax), crosses the Tropical Atlantic between 15 and 20°S from Brazil to Africa (Figures 2 and 3). The meridional Smax marks the southern flank of the Tropical Front. In the west, off Brazil, the meridional Smax is collocated with the absolute maximum of SSS, dubbed "SSS-max" by Gordon et al. (2015) [133], who pointed out that the South Atlantic is the only ocean where the SSS-max is found in the western part of the subtropical belt. Along the zonally trending meridional Smax identified in this study, the SSS decreases due east from >37.3 psu off Brazil down to nearly 36 psu off Africa (Figure 3).

The meridional Smax belt shifts north–south seasonally in sync with the north–south shifts of the Tropical Front. The Smax belt orientation (tilt) varies in sync with that of the Tropical Front. The persistence of the Smax belt, which shifts north–south seasonally while retaining its well-defined linear morphology, is suggestive of a mechanism that maintains this feature. Since our paper is squarely focused on kinematics, we cannot speculate on a possible physical mechanism that maintains the meridional Smax and that is responsible for the regular seasonal shifts of this feature that we observed in SSS data. We would only suggest that atmospheric variability is likely a key factor, as it affects cloudiness (hence solar radiation, evaporation, and eventually SSS), precipitation (directly affecting SSS), and winds (affecting evaporation and hence SSS).

3.1.7. Subtropical Frontal Zone (STFZ)

The Subtropical Frontal Zone (STFZ) consists of two tenuously connected fronts, western and eastern. The **Western Subtropical Front (WSTF)** is well defined in the western part of the South Atlantic, where it extends quasi-zonally along 30°S. The **Eastern Subtropical Front (ESTF)** is well defined in the eastern part of the South Atlantic, where it extends quasi-zonally along 35°S. The STFZ trends NW–SE across the South Atlantic, seemingly merging with the Subantarctic Front south of Africa to form a single front near 45°S.

3.1.8. Subantarctic Front (SAF)

The SAF extends quasi-zonally southeast and east of the Brazil-Malvinas Confluence along 45–48°S. The SAF joins the Polar Front between 30°W and 45°W, where both fronts extend along the northern flank of the Falkland Ridge as documented from in situ data by Peterson and Whitworth (1989) [134].

3.1.9. Meso-Scale Quasi-Meridional Tropical-Subtropical Fronts

Gradient maps (Figure 3) reveal an enigmatic ripple pattern of multiple quasi-meridional fronts extending between the Tropical Front and East Subtropical Front. This pattern covers a vast triangular area in the Tropical/Subtropical Atlantic, where the ripple field stretches due west from Africa toward Brazil. Within this ~2000-km-long area, ~20 fronts are regularly spaced ~100 km apart. The ripple pattern evolves seasonally, being best defined during the boreal winter, e.g., in January. Similar mesoscale streaky fronts can be seen elsewhere, e.g., in the SW Atlantic. However, the eastern tropical-subtropical ripple field stands out owing to its sheer size and regular structure.

3.2. Rio de la Plata Outflow

Monthly maps of SSS (Figure 4a,b) and SSS gradient magnitude (Figure 5) reveal seasonal variations of the Rio de la Plata (RP) estuarine front and seasonal alongshore migration of the RP plume. The estuarine front extends northward along the coast of Uruguay and Brazil in winter, reaching its maximum extent typically in June–July (except for October–November in 2015). In 2019, the Plata plume reached its maximum northern extent in June and persisted off SE Brazil for five months through October. The large extent and longevity of the Plata plume in winter 2019 was caused by the extremely high Plata discharge, which in turn was caused by the record-high discharge of Uruguay River. This discharge, for a few days, exceeded the Parana River discharge, whereas normally the former is about one-third of the latter (Aubriot et al., 2020 [135]; Kruk et al., 2021 [136]).

The alongshore northward propagation of the RP plume is facilitated by the persistent wintertime southerly winds. The alongshore progress of the RP plume can be traced by using the 31.0 isohaline off Uruguay, the 34.0 isohaline off the SE Brazil, or the 35.0 isohaline into the South Brazilian Bight. Piola and Romero (2004) [137] used the 33.5 isohaline to trace the diluted Plata waters.

The northernmost extent of the Plata water in the South Brazilian Bight (23–28°S) is more difficult to determine unambiguously because of freshwater discharges by numerous rivers that empty into the Bight (Marta-Almeida et al., 2021) [138]. Nonetheless, the Plata water may extend due north up to 23°S (~1500 km from the Plata estuary) during El Niño winter seasons (Campos et al., 1996) [67].

The Plata plume's extension to the south along the coast of Argentina is quite limited year-round and varies very little seasonally and interannually. The plume's front can be identified with the 33.4–33.6 isohalines (Figure 6), which is consistent with the 33.5 isohaline used by Piola and Romero (2004) [137] to track the plume's extension to the north. The preferred direction of the Plata plume spreading to the north is confirmed by numerical models. Monthly maps of SSS gradient magnitude GM (Figure 7) show that the GM peaks in the Samborombón Bay (off the coast of Argentina) year-round. This is consistent with the results obtained by Framiñan and Brown (1996) [77] from a multiyear statistical analysis of SST imagery. Our finding is interesting because the majority of studies postulate that the northern route (along the coast of Uruguay) is the dominant pathway for the Plata water spreading offshore. The southern route via the Samborombón Bay is widely considered to be minor vs. the northern route. However, the idea of the southern flow being slow and the Samborombón Bay being almost stagnant is incompatible with the year-round presence of enhanced salinity gradients, as evidenced by the SMOS data.

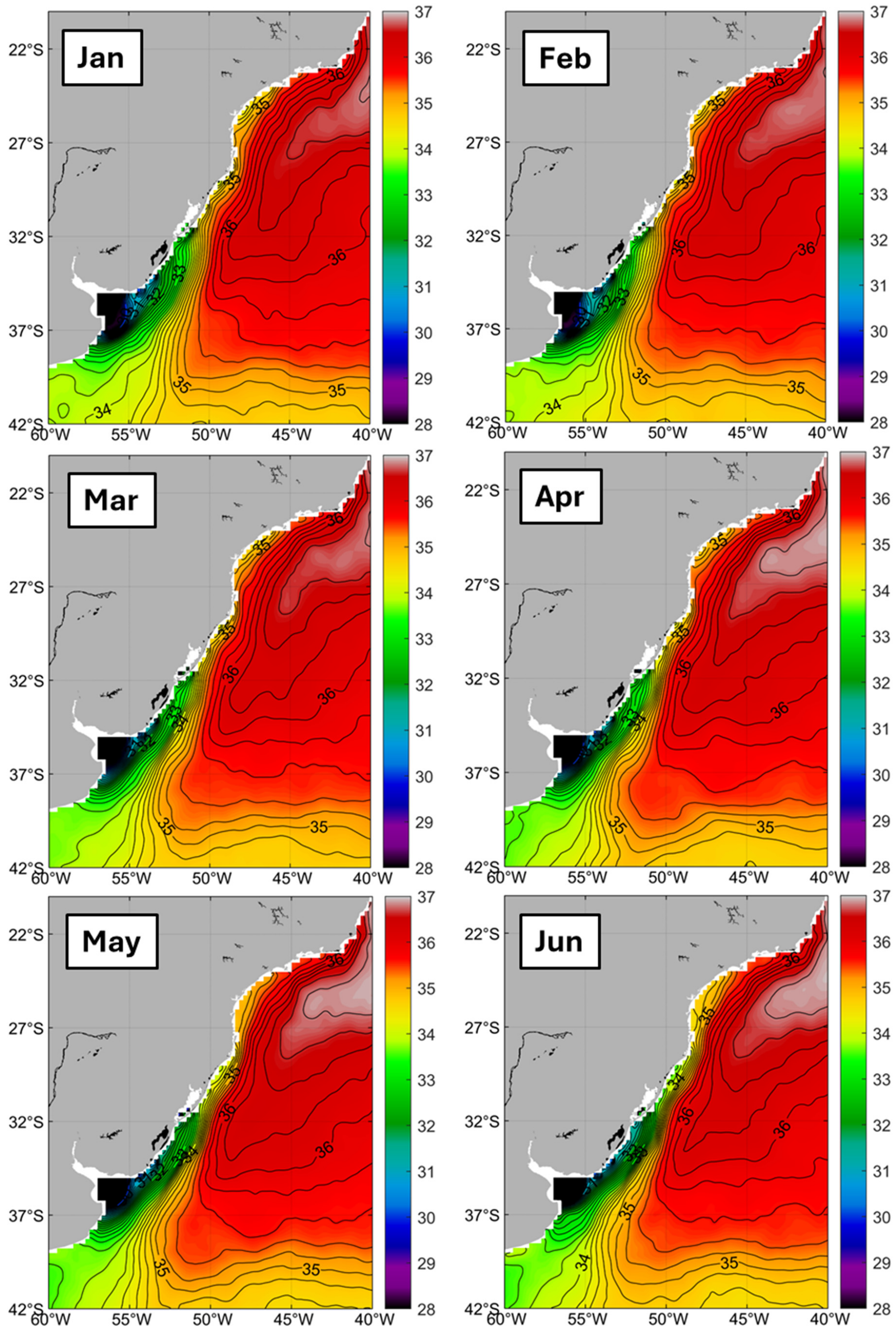

(**a**)

Figure 4. *Cont.*

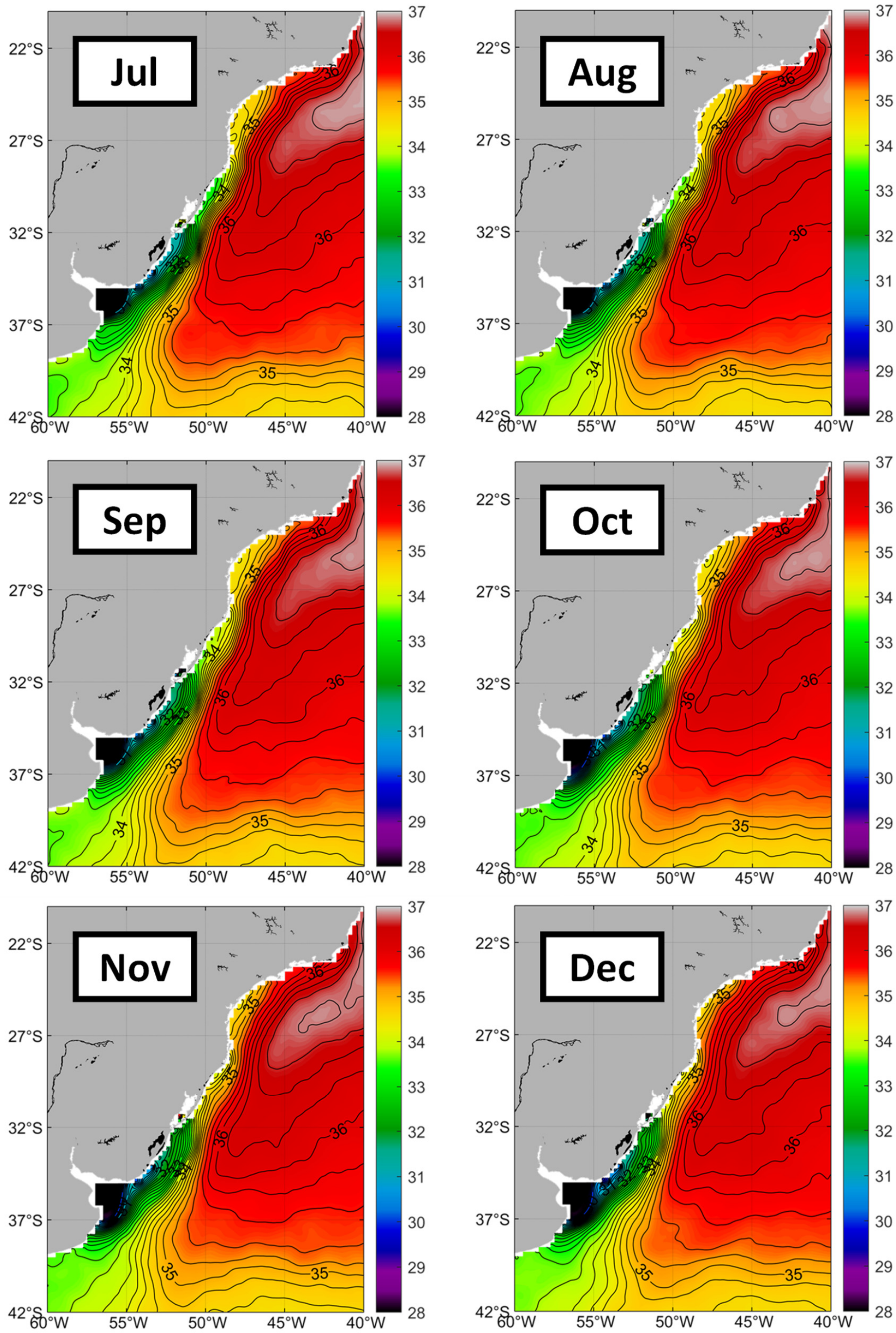

(**b**)

Figure 4. (**a**) Long-term (2011–2019) mean monthly SSS in the Rio de la Plata outflow region, January–June. (**b**) Long-term (2011–2019) mean monthly SSS in the Rio de la Plata outflow region, July–December.

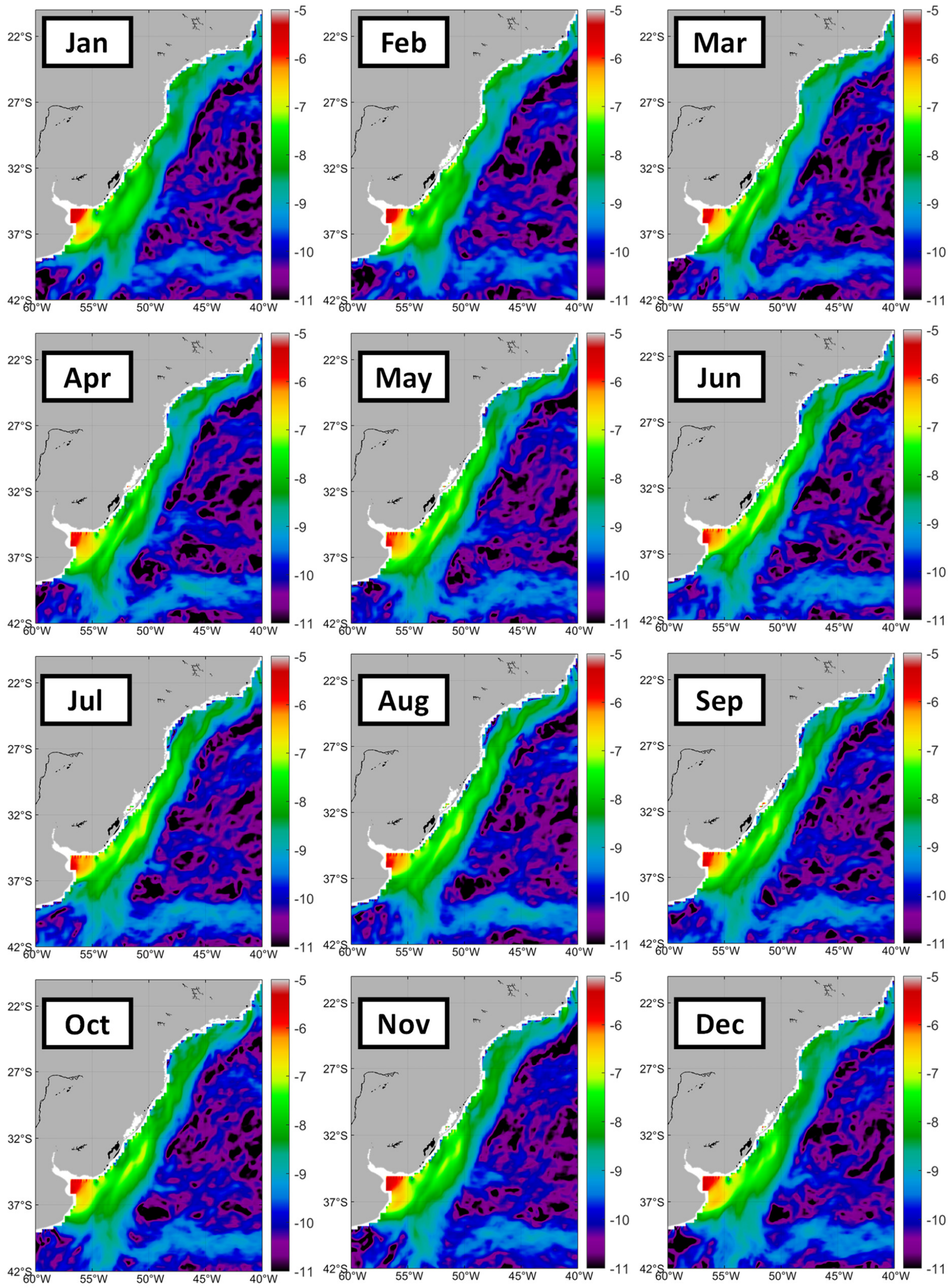

Figure 5. Long-term (2011–2019) mean monthly log-transformed gradient of SSS in the Rio de la Plata outflow region.

The low-salinity outflow from the Patos Lagoon is barely noticeable in the monthly maps of SSS (Figure 4) and SSS gradient magnitude (Figure 5), including such maps for individual months (not shown). According to the detailed aerial mapping by Burrage et al. (2008) [66], the size of the outflow bulge was 33 km × 100 km with SSS inside the bulge varying between 12 and 27 psu, ranging by ~10 psu from 18 to 28 psu across a well-defined bulge front.

The Plata estuarine front is identified with the 30.0 isohaline (Figure 6). As the season progresses, this front expands offshore in October–January and retreats inshore in February–June to stay along the Barra del Indio shoal till September. The front also changes its orientation as its western end (off the coast of Argentina) shifts from ~36°S in June to ~37°S in January, while its eastern end (off the coast of Uruguay) remains stationary year-round at ~34.5°S.

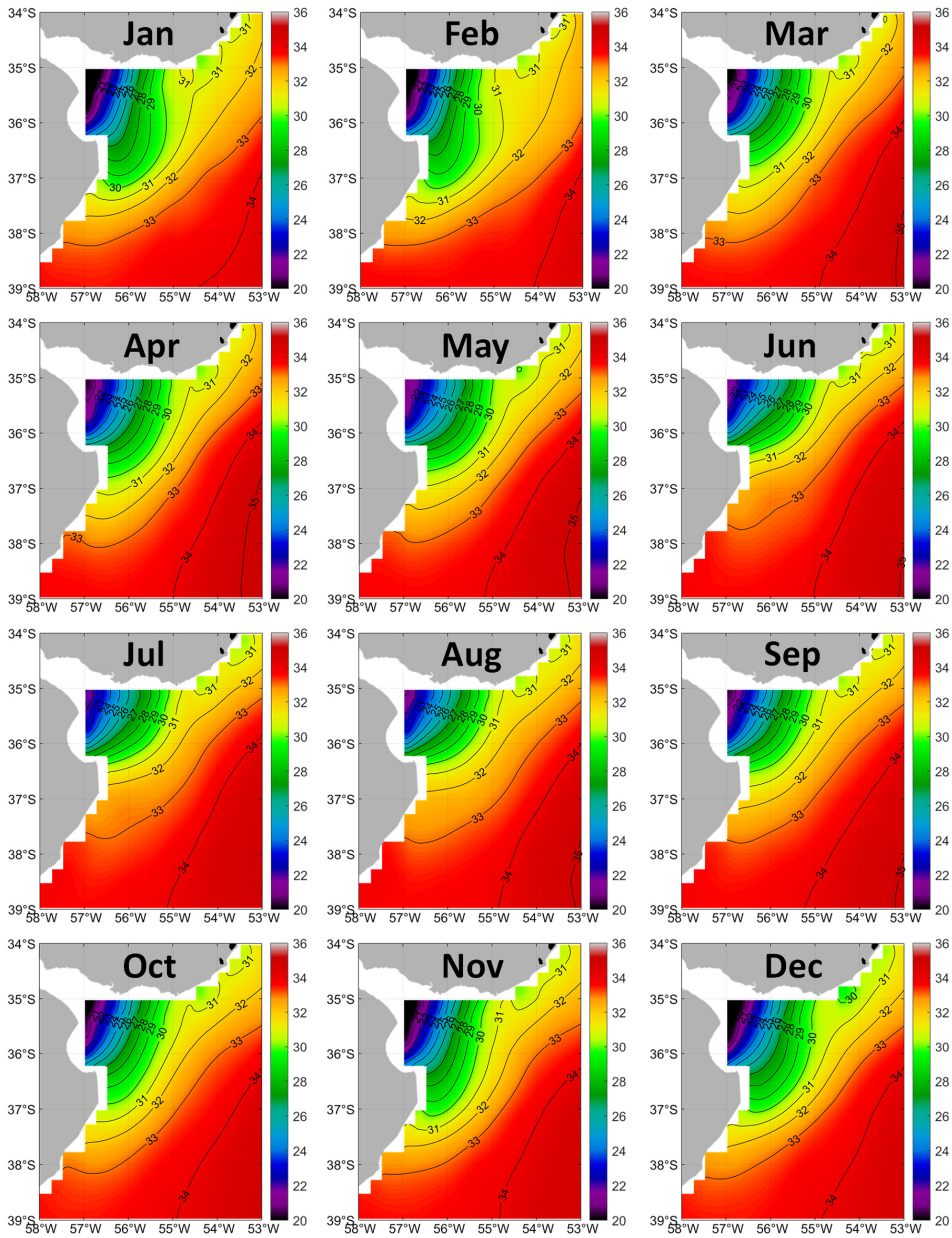

Figure 6. Long-term (2011–2019) mean monthly maps of SSS in the Plata Estuary region.

The low-salinity coastal belt's northern limit can be defined by the 34.0 isohaline, which migrates seasonally from 31.5°S in summer (November–April) to 28.5°S in winter (May–September). An alternative (broader) definition of the low-salinity coastal belt would use the 36.5 isohaline as the belt's northern boundary, which marks an interface between the low-S coastal belt and high-S subtropical gyre. The interface is not smooth. Instead, the interface is collocated with a sharp along-shore gradient of SSS (Figure 5). The low-S coastal tongue extends throughout the South Brazil Bight (SBB) year-round up to Cabo Frio (23°S, 42°W) and beyond, reaching 21°S in December–January (Figure 4). This conclusion is consistent with the climatological surface salinity map presented by Piola et al. (2018) (Figure 1a in [76]) and based on an extensive collection of in situ data. Most studies of the SBB oceanography invoke local river discharge to explain the low salinity (<34.0) of coastal waters. With the total discharge of local rivers into the SBB exceeding 4000 m^3/s (Marta-Almeida et al., 2021) [138], their impact cannot be ignored. A modeling study of river plumes in the SBB by Marta-Almeida et al. (2021) [138] revealed a low-salinity nearshore tongue propagating along the coast throughout most of the SBB up to 25.5°S and possibly occasionally up to Cabo Frio at 23°S, 42°W.

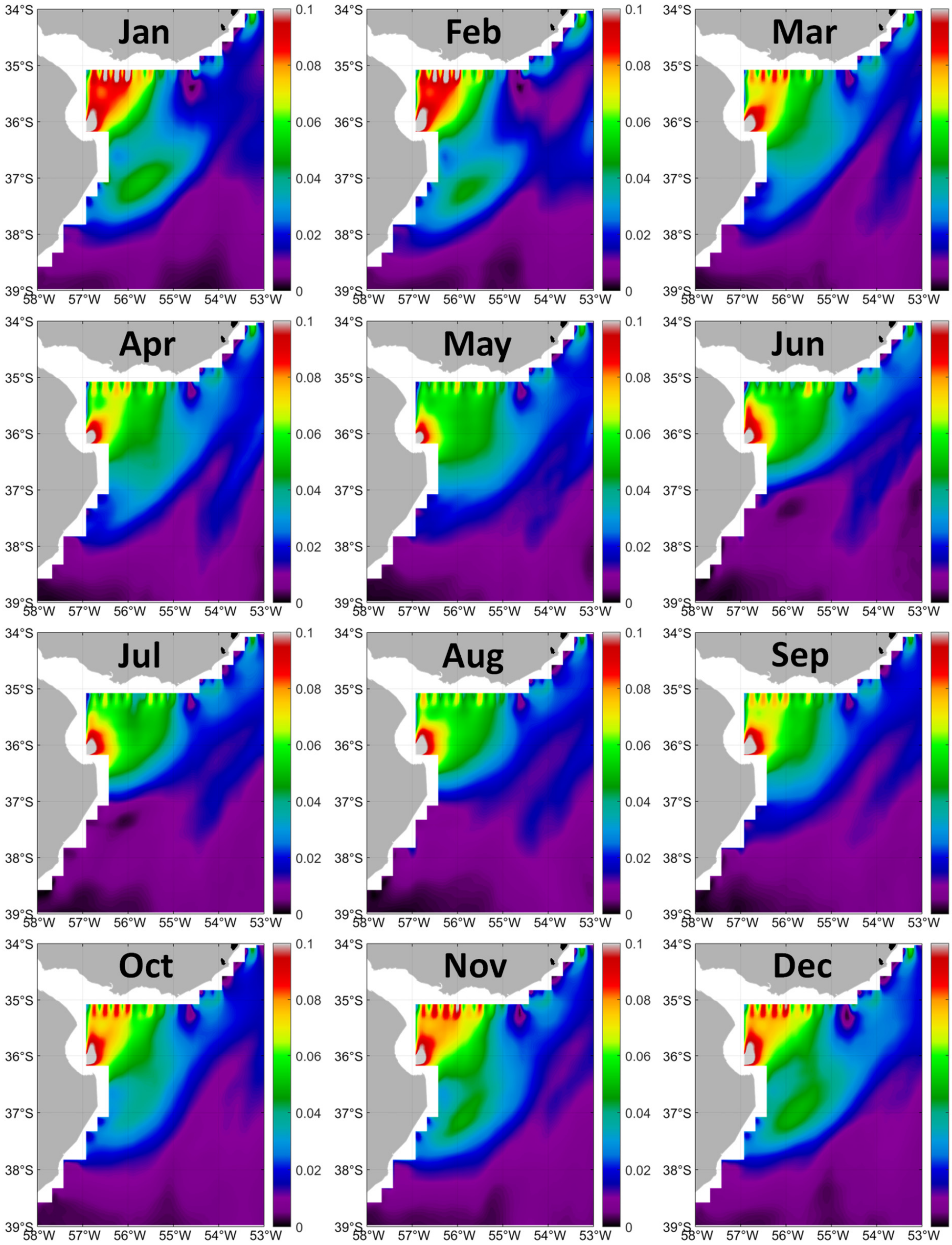

Figure 7. Long-term (2011–2019) mean monthly maps of SSS gradient magnitude in the Plata Estuary region. Red fingers along the northern flank of the estuary are likely artifacts since their scale is smaller than the resolution of the original SSS data.

3.3. Magellan Strait and Le Maire Strait Outflows

The **Magellan Strait region** in this study extends to Cape Horn (56°S, 67°W). The spatial and seasonal variability of SSS and SSS fronts in this region are illustrated by sample maps for mid-summer and mid-winter (Figure 8). The SSS field of the southern Patagonian Shelf is strongly affected by the outflow of low-salinity water from the Magellan Strait. This outflow has two sources: the Pacific Ocean off Western Patagonia, and the copious amount of local precipitation onto the Magellan Strait watershed. The low-salinity Pacific water also flows to the Eastern Patagonian Shelf along the Western Patagonia shelf break, where it is carried south and east by the Cape Horn Current (Brun et al., 2020) [81]. After bypassing Cape Horn, the Pacific water enters the Patagonian Shelf via Le Maire Strait (Brun et al., 2020) [81]. Lagrangian simulations by Guihou et al. (2020) [89] inferred a net NE-ward transport of 0.88 Sv across 51°S.

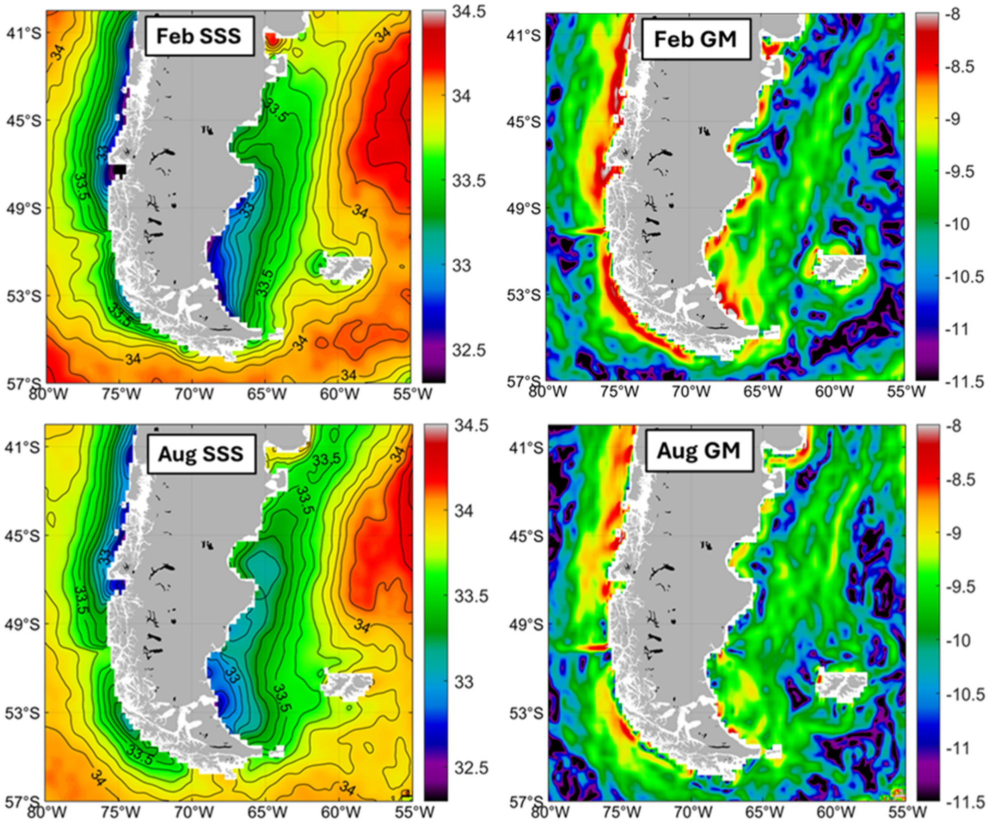

Figure 8. Long-term (2011–2019) mean monthly maps of SSS and log-transformed gradient magnitude GM of SSS in mid-summer (February) and mid-winter (August) in the Magellan Strait outflow region.

Brun et al. (2020) [81] presented an up-to-date climatological map of salinity at 20 m depth over the Patagonian Shelf from in situ data (Figure 2 in [81]). This map shows the freshwater outflow from the Magellan Strait extending north up to 43°S (see the map). The SMOS data improve this picture. According to the SMOS data, the low-salinity Magellan Strait water (S < 33.5) extends to 44°S in winter (June–July) and up to 40°S in late spring and summer (November–January). A close inspection of 108 individual monthly maps of SSS in 2011–2019 shows that the MS water occasionally extends north beyond 40°S, where it merges with the Rio de la Plata outflow. The MS outflow is bounded by a well-defined front at some distance east of the eastern entrance to the strait. This front does not appear to be terribly robust, as the MS plume extends north along the coast of Eastern Patagonia. In that respect, the MS plume qualitatively differs from the Rio de la Plata plume. Our maps do not resolve the individual flows that emanate from the Magellan Strait and Le Maire Strait. The low salinity tongue formed by the combined flow extends north alongshore, driven by the northerlies. According to Piola et al. (2018) [76], the combined low-salinity tongue eventually merges with the Rio de la Plata plume. Our maps support this conclusion. The combined low-salinity tongue forms a relatively low-intensity salinity front at its interface with ambient waters.

The low-salinity outflow from the Magellan Strait (MS) exhibits seasonal variations in its spatial extent. The MS plume's boundary can be identified with the 33.5 psu isohaline (Palma and Matano, 2012) [88], which is the same isohaline that is commonly used to delineate the Plata plume. The MS plume (defined by the 33.5 isohaline) extends north along the Patagonian coast from the Magellan Strait's eastern entrance off Punta Dungeness

(52°24′S, 68°26′W), up to 40°S in winter (June–July), but only to 44°S in spring-summer (November–January). The MS outflow is fed by a pool of low-salinity waters off western Patagonia (40°S–55°S), which is split into two parts, with a gap in between at ~50°S (Davila et al., 2002) [139]. It is the southern part of the low-salinity belt that feeds the MS throughflow.

The MS plume's characteristics (salinity, area, and northward extent) largely depend on (1) the amount, timing, and salinity of the low-salinity Pacific water coming down the Strait; (2) the amount and timing of the MS watershed precipitation; and (3) the wind stress field over the Eastern Patagonian Shelf. The vast pool of low-salinity water off Western Patagonia south of 35°S is created by copious amounts of precipitation falling on the western slopes of the Chilean Andes. This vast freshwater pool consists of two parts (lobes) separated by a wedge of more saline water at 50°S (Dávila et al., 2002) [139]. The SMOS SSS data allowed us to document this feature in detail. The monthly maps of SSS and SSS fronts (Figure 8) revealed a sharp SSS front at 50°S, which is the southern boundary of the northern lobe of low salinity, and the northern edge of the gap between the northern and southern lobes of low salinity. The gap remained absolutely stable during the 9-year study period, showing no signs of seasonal variability. Bathymetry is deemed to be the only reason for such uncanny stability of an oceanic feature. The northern lobe waxes and wanes seasonally, apparently in accordance with seasonal variations of precipitation. Using the 33.7 psu isohaline to delineate the northern lobe, its area peaks in December when the 33.7 isohaline extends west beyond 80°W. Since the northern lobe is separated from the southern lobe of low salinity, it is not clear whether the low salinity water from the north can be transported to the western entrance of the Magellan Strait. The southern lobe's seasonal variations are out of sync with the northern lobe. Indeed, the southern lobe's area peaks in March–May, and shrinks in October–January. The salinities of both lobes are quite different, with the southern lobe being much saltier than the northern lobe. Moreover, the southern lobe's minimum salinity is much higher than the minimum salinity of the Magellan Strait outflow. If the southern lobe contributes significantly to the MS outflow, the southern lobe's salinity must be substantially diluted by local precipitation within the Magellan Strait watershed, which is extremely high.

3.4. Congo River Outflow

The Congo River Plume waxes and wanes as the season progresses, as evidenced by the monthly maps of SSS and SSS gradient (Figures 9 and 10). The Plume's spatial extent and minimum axial SSS vary in sync. The Plume grows in October–March and shrinks in April–September. During the Plume's maximum extent in January–February, its axial minimum SSS (immediately offshore the river mouth) drops down to ~30 psu. During the Plume's minimum extent in July, its axial minimum SSS is ~32 psu.

The Plume Front exhibits a dominant mode of spatial orientation, which is a quasi-zonal extension to the west along 6°S, as evidenced by monthly maps of salinity gradient (Figure 10). The meridional plots of SSS along 10°E (Figure 3) document the seasonal stability of this locational mode, which varies within 1° of latitude between 5°S and 6°S. The local bathymetry south of the Congo River Canyon does not provide any clue to the front's stability. The Plume Front's spatial stability contrasts with the substantial seasonal variability of the Plume Front's intensity and strength that correlate with the Plume's seasonal variations in extent and minimum salinity noted above.

The monthly maps of SSS (Figure 9) reveal seasonal variability in the Congo River outflow. The Congo River discharge (CRD) has its main peak in summer (January–February). The CRD's main peak translates without much delay into the seasonal growth and spreading of the Plume, whose extent peaks in January–February. The absence of a significant delay is not surprising, given the extremely swift outflow of up to 2.5 m/s at the mouth. Since the Kinshasa–Brazzaville gauges are located about 500 km upstream of the mouth, the time lag between the gauges and mouth is less than three days, given the current speed of 2.5 m/s.

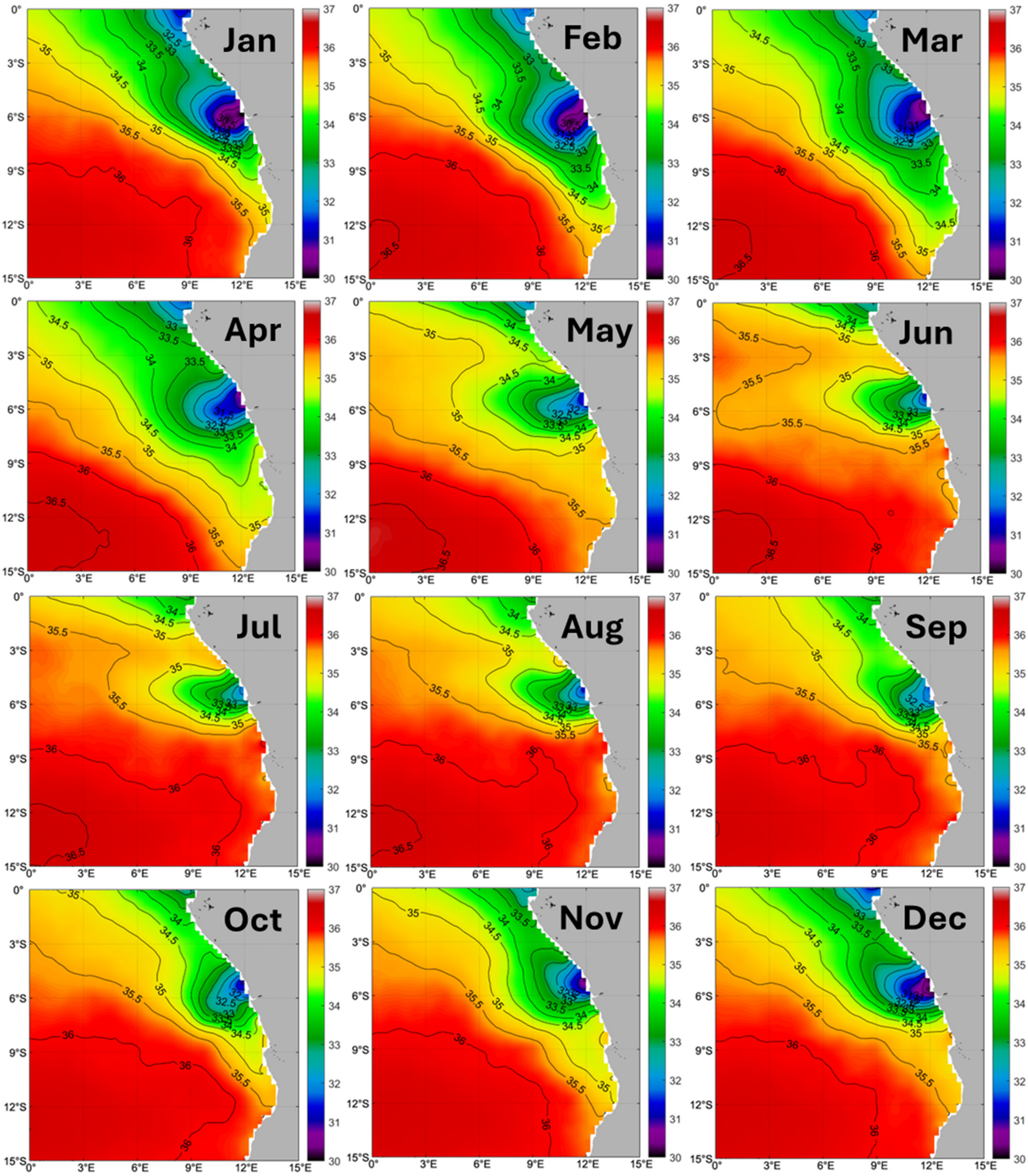

Figure 9. Long-term (2011–2019) mean monthly maps of SSS in the Congo River outflow region.

The monthly maps of SSS gradient (Figure 10) reveal the CR plume front (CRPF) and make evident the significant seasonal variability of the front's morphology, extent, location, and orientation. The outflow direction varies widely from NW alongshore, to westward offshore, to SE alongshore. The plume morphology and extent can be estimated objectively with a proper algorithm, which would be outside the scope of this study. Nonetheless, the modal location and orientation of the Plume front are apparent from monthly maps of the SSS gradient (Figure 10): most often, the plume front extends quasi-zonally along 6°S. This is the first known determination of the modal location and orientation of the Plume front.

Admittedly, this result is not quite rigorous; an objective method is needed to delineate the front and quantify its movements, orientation, and morphology.

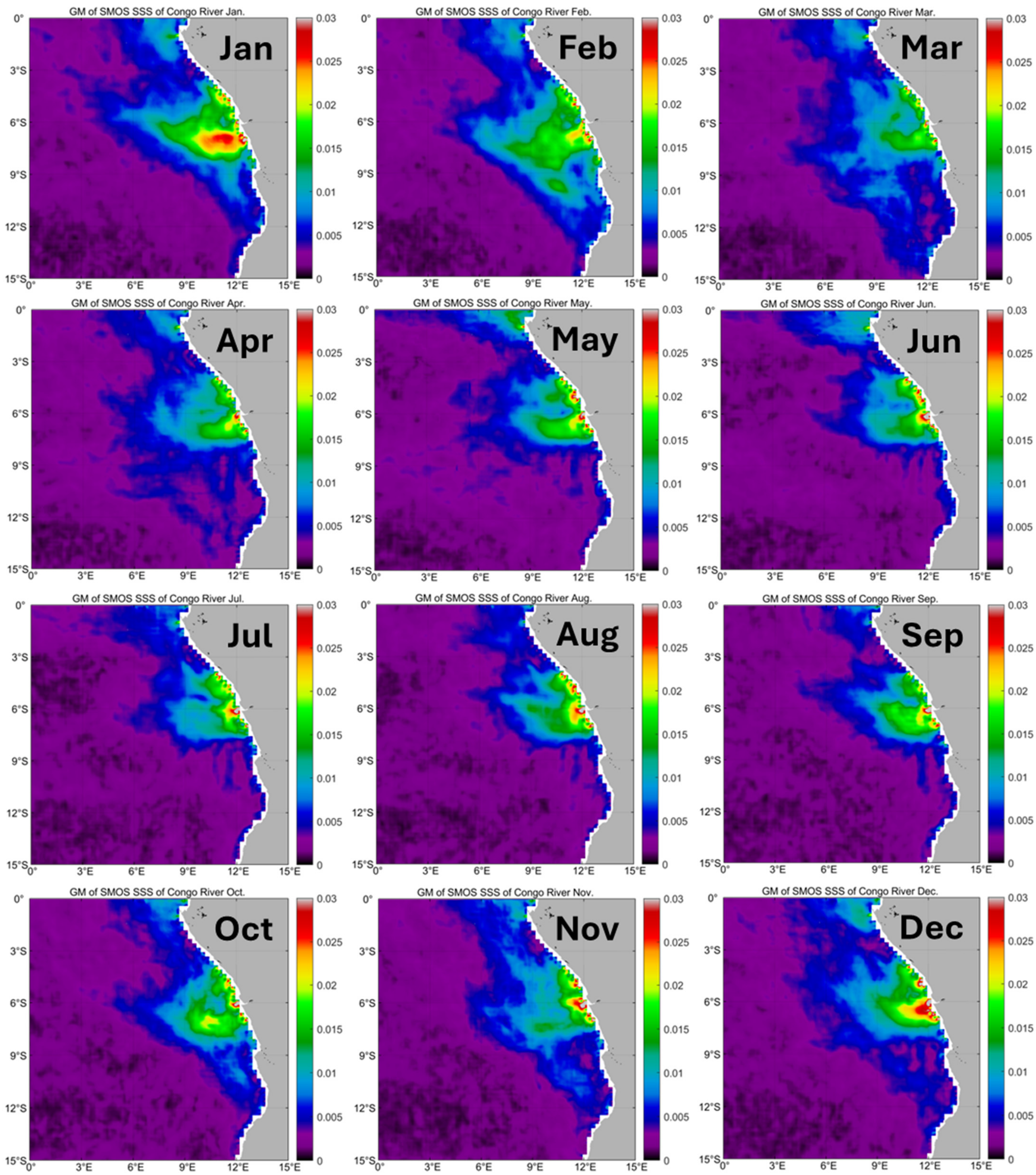

Figure 10. Long-term (2011–2019) mean monthly maps of gradient magnitude GM of SSS in the Congo River outflow region.

3.5. Angola-Benguela Front

The ABF is a quasi-zonal front, extending west from the African coast for a few hundred kilometers along 16°S, and migrating north–south seasonally. The ABF is a strong temperature front, and also a structural front, bordering from the south the sharp and shallow tropical thermocline. In the salinity field, the ABF is weak, with a cross-frontal range of a mere 0.2–0.3 psu, typically spread over a few hundred kilometers, thus never forming a sharp salinity front. Occasionally, the ABF lacks any manifestation in the salinity field, at least in the surface layer. The monthly maps of SSS and SSS gradient in the Congo–Angola–Benguela region (Figure 11) do not show any sign of enhanced SSS gradient within the zonal band of the thermal ABF (15–17°S), or immediately south of it.

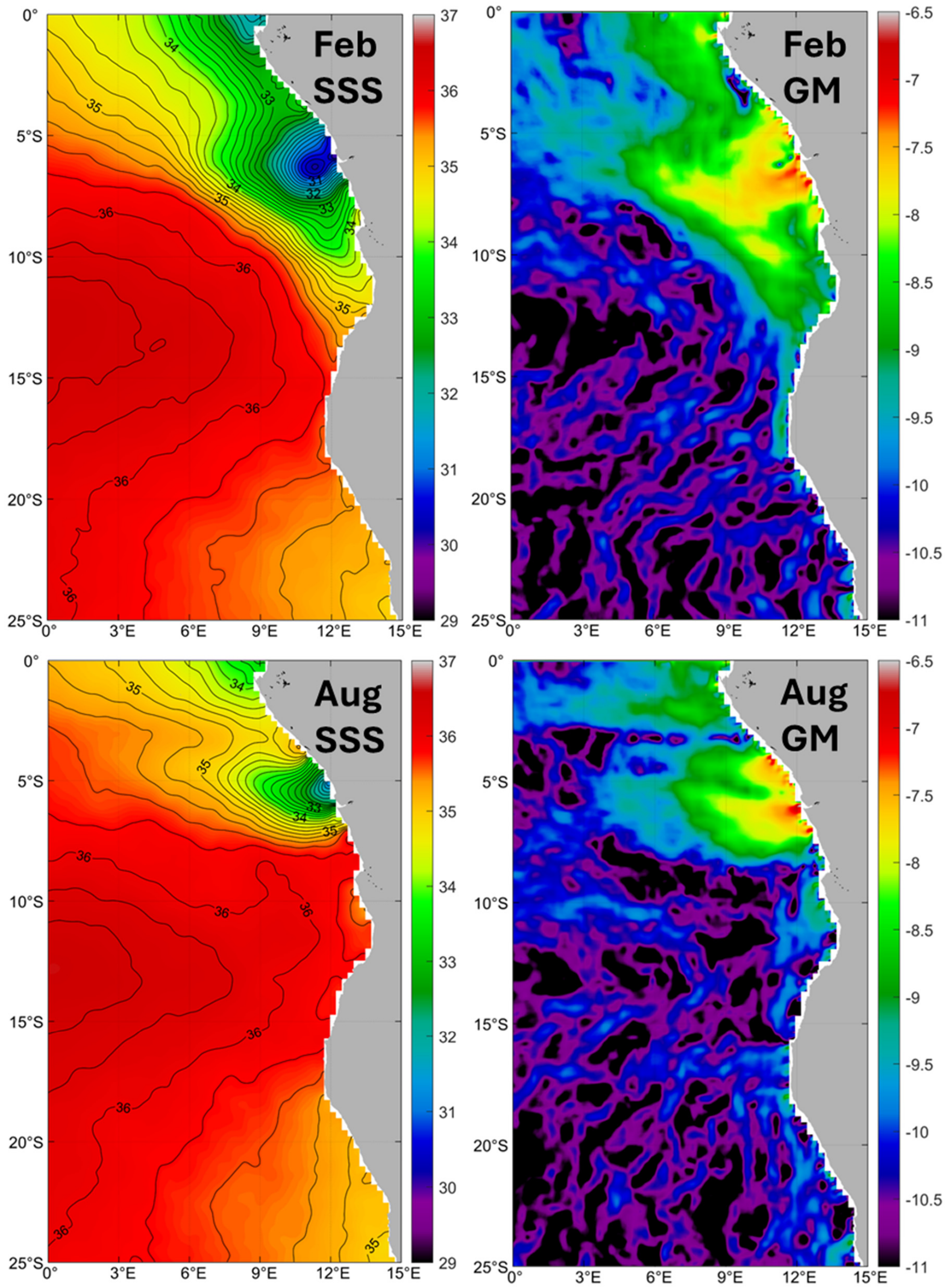

Figure 11. Long-term (2011–2019) mean monthly maps of SSS and log-transformed gradient magnitude GM of SSS in mid-summer (February) and mid-winter (August) in the Congo-Angola-Benguela region.

The most striking result is the absence of the Angola–Benguela Front (ABF) in the SSS and SSS gradient (Figure 11) fields. South of the tropical maximum of SSS, across a broad latitudinal range between 10°S and 25°S, and farther south in the SE Atlantic, the offshore SSS decreases southward in a very gradual fashion. This general north–south decreasing trend in SSS reflects a large-scale transition from tropical waters to subtropical waters. This transition manifests in the SST field as a strong thermal front (with a total cross-frontal SST range of up to 6 °C and a well-defined local maximum of SST gradient), which can be quite sharp at times. Surprisingly, unlike the great majority of ocean fronts, this thermal front is not accompanied by a local horizontal maximum in the SSS gradient field (Figure 11), a defining characteristic of a salinity front. In the SST field, the ABF manifests as a well-defined gradient maximum between 15.5°S and 17°S (Veitch et al., 2006) [54].

There is much less certainty, if any, regarding the ABF manifestation in the salinity field, especially in the surface layer, where the ABF presence is tenuous at best despite some evidence to the contrary. In the seminal paper on the ABF, Shannon et al. (1987, p. 11) [100] wrote: "Although salinity data suggest that the front may extend to a depth of at least 200 m, it is particularly marked in the upper 50 m where it can be defined in terms of both temperature and salinity", yet noted "the salinity "front" (which is admittedly weakly defined)" (*ibid.*, p. 19). The alongshore salinity data in Shannon et al. (1987) (Figure 7 in [100]) revealed a week salinity front at 17–18°S with a cross-frontal step of 0.2–0.3 psu, from 35.3–35.4 in the south to 35.6 in the north.

The April–May 1997 CTD survey of the ABF by R/V Petr Kottsov (Lass et al., 2000) [101] revealed a strong SST front, with SST ranging from 25 °C at 14°S to 16 °C at 17°S, while SSS gradually decreased from 36.2 at 14°S to 35.6 at 17°S and decreased farther south at the same rate (Figure 5 in [101]). Thus, there was no enhanced north–south gradient of SSS, and hence no SSS front, within a broad, strong SST front. Similarly, the February–March 2002 CTD survey of the ABF by FRS Africana (Ekau and Verheye, 2005) [140] documented a strong SST front, from 26 °C at 16°S to 19 °C at 18°S, with no attendant SSS front. However, a strong SSS front was found much farther south at 20°S (Figure 1 in [140]).

The absence of an SSS front can be explained by an influx of fresh water from the Gulf of Guinea, with the Congo River discharge (CRD) deemed to be the main constituent. The idea of the CRD (originated at ~6°S) affecting the ABF at 16°S—thus >1000 km away—might appear far-fetched to some researchers. For example, the CRD impact was not even mentioned by Shannon et al. (1987). Nonetheless, this idea of the CRD-ABF link seems to have been established in the literature by now. The CRD's impact can be quite dramatic during Benguela Niños. For example, in 1995, the negative SSS anomaly reached 4 psu in Angolan waters (Gammelsrød et al., 1998) [141].

The classical concept of the Angola Current carrying warm and saline tropical waters has been augmented by Mohrholz et al. (2004, pp. 1337–1339) [102]: "The Angola Current transported in its surface part less saline water from the great rivers in the north towards the ABFZ. . . . Along the continental slope the Angola Current advected warm and less saline surface waters (originating from the great rivers in the Gulf of Guinea) to 13°S, and warm tropical waters to 19°S". Thus, the influx of warm and fresh water from the Gulf of Guinea does not attenuate the thermal signature of the ABF, yet greatly reduces the salinity contrast across the ABF, which explains the absence of an SSS front within the ABF latitudinal range (15–18°S) in our results (Figures 9–11).

3.6. Benguela Upwelling Front

The dominant persistent southeasterlies blowing along the west coast of South Africa drive year-round coastal wind-induced upwelling in a vast region—Benguela Upwelling (BU)—between Cape Agulhas at 35°S and Cape Frio at 18°S. The cold upwelled water stands out in SST maps that have been extensively used in numerous studies of the BU's temporal and spatial variability. Salinity data have not been systematically utilized to date. The SMOS data clearly portray the BU region as being of low salinity and document its seasonal variability (Figure 12). The BU region includes several upwelling cells, each bordered by a local front. The entire BU region is bordered by a front called the Benguela Upwelling Front (BUF), according to von Bodungen et al. (2008) [142]. The BUF is well defined in the upper 20–40-m layer as, e.g., in May 2004, when R/V Alexander von Humboldt's zonal transect T3 along 17°S crossed the unperturbed BUF normally with SST = 17–20 °C and SSS = 35.6–35.9 (von Bodungen et al., 2008) (Figure 6 in [142]). The monthly maps of SSS gradient magnitude GM (Figure 12) reveal either a single salinity front or numerous salinity fronts that comprise the BUF.

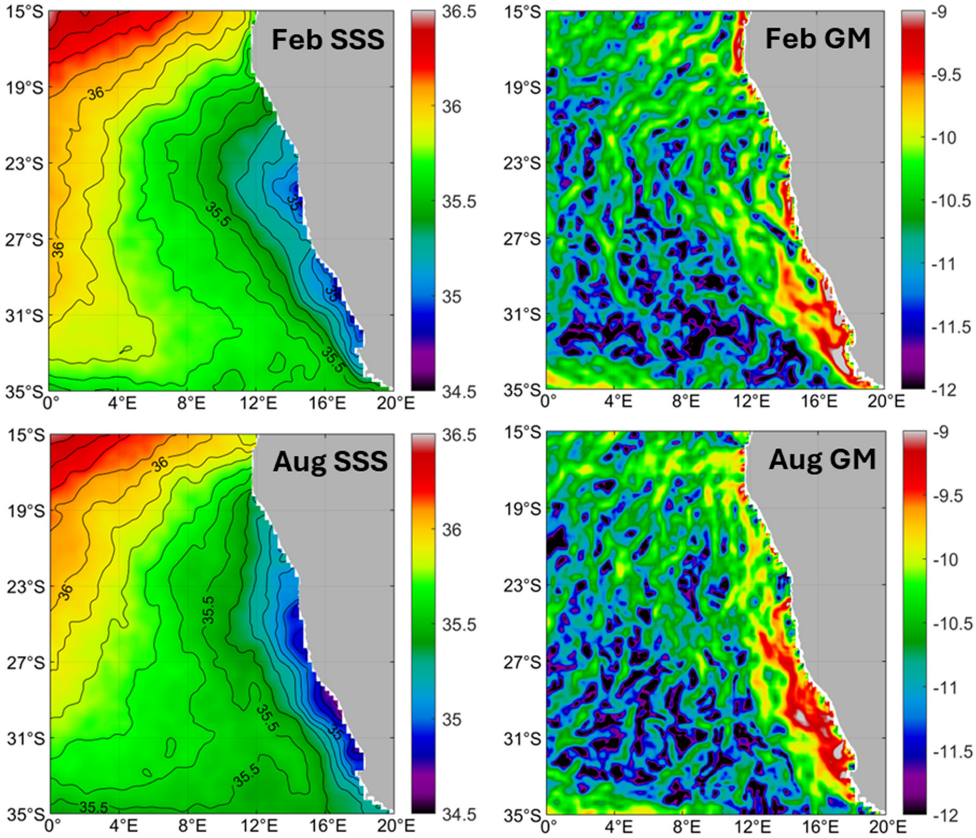

Figure 12. Long-term (2011–2019) mean monthly maps of SSS and log-transformed gradient magnitude GM of SSS in mid-summer (February) and mid-winter (August) in the Benguela Upwelling region.

4. Discussion

Large-scale open-ocean fronts: The SMOS SSS data revealed a rich pattern of salinity fronts in the South Atlantic, including a few newly identified features. Perhaps the most important frontal zone that has been reliably documented during this study is the Tropical Front, which has not been distinguished in the South Atlantic in previous satellite studies of salinity fronts (listed in Section 1 and Table 1). Another feature of interest is the discontinuity of the Subtropical Frontal Zone (STFZ), previously noted by Graham and de Boer (2013) [31]. The STFZ was found to consist of two major frontal zones (Western and Eastern STF), both quasi-zonal, yet offset from one another by up to 5° of latitude (roughly 500 km). This finding will likely revive the discussion of continuity (or discontinuity) of the STFZ across the South Atlantic. In this respect, Burls and Reason (2006, p. 10) [21] wrote: "West of about 15°W, the satellite data analyzed here suggests little evidence of continuous frontal features associated with the Subtropical Front extending across the basin. By contrast, Deacon [1982] and Peterson and Stramma [1991] used hydrographic data to infer that such a continuous feature does exist across the basin".

Freshwater pools and ITCZ: Reul et al. (2014) [2] pointed out the importance of monitoring the space-time variability of freshwater pools created by copious amounts of precipitation in the Inter-Tropical Convergence Zone, ITCZ. The ITCZ freshwater pools are likely bordered by salinity fronts in a pattern similar to that in the equatorial Indian Ocean, where, according to Nyadjro and Subrahmanyam (2016, p. 146) [11], "Strong salinity fronts are observed along the equatorial region, with meridional migration of the fronts following the migration of the Intertropical Convergence Zone (ITCZ)". In the equatorial Atlantic, the ITCZ and associated salinity fronts are located north of the equator, outside our study area.

The **Angola–Benguela Front (ABF)** is traditionally recognized as a boundary between the southward flowing warm waters of the Angola Current and northward flowing cold waters of the Benguela Current (Shannon et al., 1987) [100]. The above traditional concept of the ABF as a confluence of two meridional currents is a simplification. Complications come from both sides. In the north, the Congo River's summertime peak discharge feeds the Congo River plume extending south alongshore toward the ABF. In the south, the Benguela Upwelling brings cold and less saline water to the surface layer, where this water spreads north alongshore toward the ABF. Thus, the large-scale salinity pattern consists of three water masses: (1) low-salinity water of the Congo River in the north; (2) low-salinity water of the Benguela Upwelling in the south; and (3) tropical high-salinity water in-between. The monthly maps of SSS in the Congo-Angola–Benguela region (Figures 9–12) clearly document the significant seasonal variability of the above three-component SSS pattern. The summertime (January–April) southward alongshore spreading of the Congo River water is apparent in every summer except 2013 and 2017, with the most extensive spreading event in 2016. Perhaps not coincidentally, this was the year of a Benguela Niño. The Benguela Upwelling's intensity and extent are known to peak in winter (July–September) when the southerly winds pick up. The northward alongshore spreading of upwelled water normally follows upwelling episodes. The monthly maps of SSS in the Benguela Upwelling region (Figure 12) portray the seasonal northward spreading of low-salinity water brought by upwelling and alongshore advection.

Validation: A rigorous validation study would involve comparisons with remote sensing SSS data from other satellite missions (Aquarius and SMAP) and in situ data from a variety of platforms (oceanographic stations, underway CTDs, Argo buoys etc.). Such a massive endeavor is outside the scope of this paper, yet is planned for the near future. Meanwhile, ad hoc comparisons with published SSS data attest to the accuracy of the SMOS SSS data provided by the BEC and documented by Olmedo et al. (2021) [118]. For example, our definitions of the Rio de la Plata plume front and Magellan plume front from SMOS SSS data are consistent (within 0.1 psu) with definitions used in numerous studies based on in situ data (Piola et al., 2018 [76]; Palma and Matano, 2012 [88]). In the tropics, the maximum salinity (off Brazil) of meridional Smax from SMOS SSS data is virtually the same (within 0.1 psu) as the collocated SSS-max in the monthly climatology by Aubone et al. (2021) [143]. The Congo River outflow is delineated by a salinity front with the axial SSS similar to the one adopted by previous researchers (e.g., Houndegnonto et al., 2021 [35]). In the Benguela Current system, our criterion for the delineation of the upwelled water from SMOS SSS data is consistent with the criteria used in numerous studies based on in situ data (e.g., Ekau and Verheye, 2005 [140]).

5. Conclusions

We conducted a systematic study of sea surface salinity (SSS) fronts in the South Atlantic using satellite SMOS SSS data from 2011–2019. We produced and analyzed monthly climatology of SSS fronts from high-resolution (1/20°) daily SSS data generated at the Barcelona Expert Center of Remote Sensing (BEC). The daily data were averaged on a monthly basis (largely to mitigate some artifacts, e.g., faint horizontal stripes); then, monthly data were used in the analysis. The Belkin–O'Reilly algorithm (BOA) was used to generate gradients of SSS after filtering out impulse/dot/salt-and-pepper noise, while preserving high-gradient zones identified with salinity fronts. To facilitate feature recognition in satellite imagery, the SSS gradient magnitude GM generated by the BOA algorithm was log-transformed. Experiments have shown that log-transformation of original SSS data slightly improves the visual contrast of gradient maps, although this additional preprocessing step is not critical, while log-transformation of the gradient is crucial. The enhanced visual contrast of the gradient maps revealed a few newly identified features, such as a giant 2000 km-long ripple field of quasi-meridional mesoscale (100 km wave length) striations in the tropical-subtropical Atlantic, and a narrow linear band of meridional SSS maximum south of the Tropical Front. Large-scale open-ocean salinity fronts are stable and do not substantially change seasonally, except for the equatorial belt and, to some extent, the Tropical Front, which shifts seasonally in the north–south direction and also changes its orientation (non-zonal tilt). Strong fronts border low-salinity regions maintained by the Rio de la Plata discharge, Magellan Strait outflow, Congo River discharge, and Benguela Upwelling. In the SW Atlantic, the Plata plume expands northward in winter (June–July), reaching into the South Brazilian Bight, up to Cabo Frio (23°S) and beyond. The inner Plata front moves in and out seasonally. The Magellan Strait outflow expands northward in winter (June–July) from 53°S up to 39–40°S and sometimes beyond, approaching the Plata outflow. In the SE Atlantic, the Congo River plume spreads radially from the river mouth, with the outflow direction and areal extent varying seasonally. The plume is often bordered from the south by a quasi-zonal front along 6°S. The diluted Congo River water spreads southward seasonally over a 1000 km distance down to the Angola–Benguela Front at 16°S (mean position). The Benguela Upwelling is bordered by a quasi-meridional front, which extends north alongshore up to 20°S, where the low-salinity Benguela Upwelling water forms a salinity front, which is separate from the thermal Angola–Benguela Front at 16°S. The high-salinity tropical water ("Angola water") forms a wedge between the diluted Congo River water and low-salinity Benguela Upwelling water. This high-salinity wedge is bordered by salinity fronts that migrate north–south seasonally.

Author Contributions: Conceptualization, I.M.B.; Methodology, I.M.B.; Software, X.-T.S.; Validation, I.M.B. and X.-T.S.; Formal analysis, I.M.B.; Investigation, I.M.B. and X.-T.S.; Data curation, X.-T.S.; Writing—original draft, I.M.B.; Writing—review & editing, I.M.B.; Visualization, I.M.B. and X.-T.S.; Supervision, I.M.B. All authors have read and agreed to the published version of the manuscript.

Funding: X.-T.S. is funded by Science and Technology Project of Zhoushan, Grant No.: 2023C41020.

Data Availability Statement: The data and results are available from the corresponding author upon request.

Acknowledgments: We appreciate the great work done at the Barcelona Expert Center of Remote Sensing (BEC) that made this study possible. The original manuscript was improved thanks to the comments made by two anonymous reviewers.

Conflicts of Interest: The authors declare no conflicts of interest.

References

1. Boutin, J.; Yueh, S.; Bindlish, R.; Chan, S.; Entekhabi, D.; Kerr, Y.; Kolodziejczyk, N.; Lee, T.; Reul, N.; Zribi, M. Soil moisture and sea surface salinity derived from satellite-borne sensors. *Surv. Geophys.* **2023**, *44*, 1449–1487. [CrossRef]
2. Reul, N.; Fournier, S.; Boutin, J.; Hernandez, O.; Maes, C.; Chapron, B.; Alory, G.; Quilfen, Y.; Tenerelli, J.; Morisset, S.; et al. Sea surface salinity observations from space with the SMOS satellite: A new means to monitor the marine branch of the water cycle. *Surv. Geophys.* **2014**, *35*, 681–722. [CrossRef]
3. Boutin, J.; Vergely, J.L.; Marchand, S.; d'Amico, F.; Hasson, A.; Kolodziejczyk, N.; Reul, N.; Reverdin, G.; Vialard, J. New SMOS Sea Surface Salinity with reduced systematic errors and improved variability. *Remote Sens. Environ.* **2018**, *214*, 115–134. [CrossRef]
4. Vinogradova, N.; Lee, T.; Boutin, J.; Drushka, K.; Fournier, S.; Sabia, R.; Stammer, D.; Bayler, E.; Reul, N.; Gordon, A.; et al. Satellite salinity observing system: Recent discoveries and the way forward. *Front. Mar. Sci.* **2019**, *6*, 243. [CrossRef]
5. Reul, N.; Grodsky, S.A.; Arias, M.; Boutin, J.; Catany, R.; Chapron, B.; d'Amico, F.; Dinnat, E.; Donlon, C.; Fore, A.; et al. Sea surface salinity estimates from spaceborne L-band radiometers: An overview of the first decade of observation (2010–2019). *Remote Sens. Environ.* **2020**, *242*, 111769. [CrossRef]
6. Boutin, J.; Reul, N.; Köhler, J.; Martin, A.; Catany, R.; Guimbard, S.; Rouffi, F.; Vergely, J.L.; Arias, M.; Chakroun, M.; et al. Satellite-based sea surface salinity designed for ocean and climate studies. *J. Geophys. Res. Ocean.* **2021**, *126*, e2021JC017676. [CrossRef]
7. Qu, T.D.; Song, Y.T.; Maes, C. Sea surface salinity and barrier layer variability in the equatorial Pacific as seen from Aquarius and Argo. *J. Geophys. Res. Ocean.* **2014**, *119*, 15–29. [CrossRef]
8. Kao, H.Y.; Lagerloef, G.S.E. Salinity fronts in the tropical Pacific Ocean. *J. Geophys. Res. Ocean.* **2015**, *120*, 1096–1106. [CrossRef] [PubMed]
9. Yu, L.S. Sea-surface salinity fronts and associated salinity-minimum zones in the tropical ocean. *J. Geophys. Res. Ocean.* **2015**, *120*, 4205–4225. [CrossRef]

10. Melnichenko, O.; Hacker, P.; Maximenko, N.; Lagerloef, G.; Potemra, J. Optimum interpolation analysis of Aquarius sea surface salinity. *J. Geophys. Res. Ocean.* **2016**, *121*, 602–616. [CrossRef]
11. Nyadjro, E.S.; Subrahmanyam, B. Spatial and temporal variability of central Indian Ocean salinity fronts observed by SMOS. *Remote Sens. Environ.* **2016**, *180*, 146–153. [CrossRef]
12. Asto, C.; Chaigneau, A.; Gutiérrez, D. Spatio-temporal variability of the equatorial front in the eastern tropical Pacific from remote sensing salinity data (2010–2015). *Deep-Sea Res. Part II* **2019**, *169–170*, 104640. [CrossRef]
13. Bao, S.L.; Wang, H.Z.; Zhang, R.; Yan, H.Q.; Chen, J.; Bai, C.Z. Application of phenomena-resolving assessment methods to satellite sea surface salinity products. *Earth Space Sci.* **2021**, *8*, e2020EA001410. [CrossRef]
14. Vazquez-Cuervo, J.; García-Reyes, M.; Gómez-Valdés, J. Identification of sea surface temperature and sea surface salinity fronts along the California Coast: Application using Saildrone and satellite derived products. *Remote Sens.* **2023**, *15*, 484. [CrossRef]
15. Legeckis, R. A survey of worldwide sea surface temperature fronts detected by environmental satellites. *J. Geophys. Res. Ocean.* **1978**, *83*, 4501–4522. [CrossRef]
16. Allega, L.; Pisoni, J.P.; Cozzolino, E.; Maenza, R.A.; Piccolo, M.C. The variability of sea surface temperature in the Patagonian Shelf Argentina, from 35 years of satellite information. *Int. J. Remote Sens.* **2021**, *42*, 6090–6106. [CrossRef]
17. Artana, C.; Lellouche, J.M.; Park, Y.H.; Garric, G.; Koenig, Z.; Sennéchael, N.; Ferrari, R.; Piola, A.R.; Saraceno, M.; Provost, C. Fronts of the Malvinas Current System: Surface and subsurface expressions revealed by satellite altimetry, Argo floats, and Mercator operational model outputs. *J. Geophys. Res. Ocean.* **2018**, *123*, 5261–5285. [CrossRef]
18. Barré, N.; Provost, C.; Saraceno, M. Spatial and temporal scales of the Brazil–Malvinas Current confluence documented by simultaneous MODIS Aqua 1.1-km resolution SST and color images. *Adv. Space Res.* **2006**, *37*, 770–786. [CrossRef]
19. Billany, W.; Swart, S.; Hermes, J.; Reason, C.J.C. Variability of the Southern Ocean fronts at the Greenwich Meridian. *J. Mar. Syst.* **2010**, *82*, 304–310. [CrossRef]
20. Bouali, M.; Sato, O.T.; Polito, P.S. Temporal trends in sea surface temperature gradients in the South Atlantic Ocean. *Remote Sens. Environ.* **2017**, *194*, 100–114. [CrossRef]
21. Burls, N.J.; Reason, C.J.C. Sea surface temperature fronts in the midlatitude South Atlantic revealed by using microwave satellite data. *J. Geophys. Res. Ocean.* **2006**, *111*, C08001. [CrossRef]
22. Castellanos, P.; Olmedo, E.; Pelegrí, J.L.; Turiel, A.; Campos, E.J.D. Seasonal variability of retroflection structures and transports in the Atlantic Ocean as inferred from satellite-derived salinity maps. *Remote Sens.* **2019**, *11*, 802. [CrossRef]
23. Chao, Y.; Farrara, J.D.; Schumann, G.; Andreadis, K.M.; Moller, D. Sea surface salinity variability in response to the Congo River discharge. *Cont. Shelf Res.* **2015**, *99*, 35–45. [CrossRef]
24. Chen, H.H.; Qi, Y.; Wang, Y.; Chai, F. Seasonal variability of SST fronts and winds on the southeastern continental shelf of Brazil. *Ocean Dyn.* **2019**, *69*, 1387–1399. [CrossRef]
25. da Silveira, I.C.; Pereira, F.; Flierl, G.R.; Simoes-Sousa, I.T.; Palóczy, A.; Borges-Silva, M.; Rocha, C.B. The Brazil Current quasi-stationary unstable meanders at 22°S–23°S. *Prog. Oceanogr.* **2023**, *210*, 102925. [CrossRef]
26. Dencausse, G.; Arhan, M.; Speich, S. Is there a continuous Subtropical Front south of Africa? *J. Geophys. Res. Ocean.* **2011**, *116*, C02027. [CrossRef]
27. Dong, S.; Sprintall, J.; Gille, S.T. Location of the Antarctic polar front from AMSR-E satellite sea surface temperature measurements. *J. Phys. Oceanogr.* **2006**, *36*, 2075–2089. [CrossRef]
28. Franco, B.C.; Piola, A.R.; Rivas, A.L.; Baldoni, A.; Pisoni, J.P. Multiple thermal fronts near the Patagonian shelf break. *Geophys. Res. Lett.* **2008**, *35*, L02607. [CrossRef]
29. Franco, B.C.; Ruiz-Etcheverry, L.A.; Marrari, M.; Piola, A.R.; Matano, R.P. Climate change Impacts on the Patagonian shelf break front. *Geophys. Res. Lett.* **2022**, *49*, e2021GL096513. [CrossRef]
30. Freeman, N.M.; Lovenduski, N.S. Mapping the Antarctic Polar Front: Weekly realizations from 2002 to 2014. *Earth Syst. Sci. Data* **2016**, *8*, 191–198. [CrossRef]
31. Graham, R.M.; de Boer, A.M. The Dynamical Subtropical Front. *J. Geophys. Res. Ocean.* **2013**, *118*, 5676–5685. [CrossRef]
32. Guerrero, R.A.; Piola, A.R.; Fenco, H.; Matano, R.P.; Combes, V.; Chao, Y.; James, C.; Palma, E.D.; Saraceno, M.; Strub, P.T. The salinity signature of the cross-shelf exchanges in the Southwestern Atlantic Ocean: Satellite observations. *J. Geophys. Res. Ocean.* **2014**, *119*, 7794–7810. [CrossRef] [PubMed]
33. Hopkins, J.; Lucas, M.; Dufau, C.; Sutton, M.; Stum, J.; Lauret, O.; Channelliere, C. Detection and variability of the Congo River plume from satellite derived sea surface temperature, salinity, ocean colour and sea level. *Remote Sens. Environ.* **2013**, *139*, 365–385. [CrossRef]
34. Hösen, E.; Möller, J.; Jochumsen, K.; Quadfasel, D. Scales and properties of cold filaments in the Benguela upwelling system off Lüderitz. *J. Geophys. Res. Ocean.* **2016**, *121*, 1896–1913. [CrossRef]
35. Houndegnonto, O.J.; Kolodziejczyk, N.; Maes, C.; Bourlès, B.; Da-Allada, C.Y.; Reul, N. Seasonal variability of freshwater plumes in the eastern Gulf of Guinea as inferred from satellite measurements. *J. Geophys. Res. Ocean.* **2021**, *126*, e2020JC017041. [CrossRef]
36. Kim, Y.S.; Orsi, A.H. On the variability of Antarctic Circumpolar Current fronts inferred from 1992–2011 altimetry. *J. Phys. Oceanogr.* **2014**, *44*, 3054–3071. [CrossRef]
37. Legeckis, R.; Gordon, A.L. Satellite observations of the Brazil and Falkland currents—1975 1976 and 1978. *Deep-Sea Res.* **1982**, *29*, 375–401. [CrossRef]

38. Lorenzzetti, J.A.; Stech, J.L.; Mello Filho, W.L.; Assireu, A.T. Satellite observation of Brazil Current inshore thermal front in the SW South Atlantic: Space/time variability and sea surface temperatures. *Cont. Shelf Res.* **2009**, *29*, 2061–2068. [CrossRef]
39. Luko, C.D.; da Silveira, I.C.A.; Simoes-Sousa, I.T.; Araujo, J.M.; Tandon, A. Revisiting the Atlantic South Equatorial Current. *J. Geophys. Res. Ocean.* **2021**, *126*, e2021JC017387. [CrossRef]
40. Lutjeharms, J.R.E.; Meeuwis, J.M. The extent and variability of South-East Atlantic upwelling. *S. Afr. J. Mar. Sci.* **1987**, *5*, 51–62. [CrossRef]
41. Lutjeharms, J.R.E.; Valentine, H.R.; van Ballegooyen, R.C. On the Subtropical Convergence in the South Atlantic Ocean. *S. Afr. J. Sci.* **1993**, *89*, 552–559.
42. Martins, M.S.; Stammer, D. Interannual variability of the Congo River Plume-induced sea surface salinity. *Remote Sens.* **2022**, *14*, 1013. [CrossRef]
43. Meeuwis, J.M.; Lutjeharms, J.R.E. Surface thermal characteristics of the Angola-Benguela front. *S. Afr. J. Mar. Sci.* **1990**, *9*, 261–279. [CrossRef]
44. Meeuwis, J.M. Geographic Characteristics of Circulation Patterns and Features in the South Atlantic and South Indian Oceans Using Satellite Remote Sensing. Ph.D. Thesis, University of Johannesburg, Johannesburg, South Africa, 1991; 418p. Available online: https://hdl.handle.net/10210/10106 (accessed on 14 January 2024).
45. Moore, J.K.; Abbott, M.R.; Richman, J.G. Variability in the location of the Antarctic Polar Front (90°–20°W) from satellite sea surface temperature data. *J. Geophys. Res. Ocean.* **1997**, *102*, 27825–27833. [CrossRef]
46. Moore, J.K.; Abbott, M.R.; Richman, J.G. Location and dynamics of the Antarctic Polar Front from satellite sea surface temperature data. *J. Geophys. Res. Ocean.* **1999**, *104*, 3059–3073. [CrossRef]
47. Olson, D.B.; Podestá, G.P.; Evans, R.H.; Brown, O.B. Temporal variations in the separation of Brazil and Malvinas Currents. *Deep Sea Res.* **1988**, *35*, 1971–1990. [CrossRef]
48. Piola, A.R.; Romero, S.I.; Zajaczkovski, U. Space-time variability of the Plata plume inferred from ocean color. *Cont. Shelf Res.* **2008**, *28*, 1556–1567. [CrossRef]
49. Rivas, A.L. Spatial and temporal variability of satellite-derived sea surface temperature in the southwestern Atlantic Ocean. *Cont. Shelf Res.* **2010**, *30*, 752–760. [CrossRef]
50. Rivas, A.L.; Pisoni, J.P. Identification, characteristics and seasonal evolution of surface thermal fronts in the Argentinean Continental Shelf. *J. Mar. Syst.* **2010**, *79*, 134–143. [CrossRef]
51. Ruiz-Etcheverry, L.A.; Saraceno, M. Sea level trend and fronts in the South Atlantic Ocean. *Geosciences* **2020**, *10*, 218. [CrossRef]
52. Saraceno, M.; Provost, C.; Piola, A.R.; Bava, J.; Gagliardini, A. Brazil Malvinas Frontal System as seen from 9 years of advanced very high resolution radiometer data. *J. Geophys. Res. Ocean.* **2004**, *109*, C05027. [CrossRef]
53. Saraceno, M.; Provost, C.; Piola, A.R. On the relationship between satellite-retrieved surface temperature fronts and chlorophyll *a* in the western South Atlantic. *J. Geophys. Res. Ocean.* **2005**, *110*, C11016. [CrossRef]
54. Veitch, J.A.; Florenchie, P.; Shillington, F.A. Seasonal and interannual fluctuations of the Angola-Benguela Frontal Zone (ABFZ) using 4.5 km resolution satellite imagery from 1982 to 1999. *Int. J. Remote Sens.* **2006**, *27*, 987–998. [CrossRef]
55. Wang, Z.; Chen, G.; Han, Y.; Ma, C.Y.; Lv, M. Southwestern Atlantic Ocean fronts detected from satellite-derived SST and chlorophyll. *Remote Sens.* **2021**, *13*, 4402. [CrossRef]
56. Wang, Z.; Chen, G.; Ma, C.Y.; Liu, Y.L. Southwestern Atlantic Ocean fronts detected from the fusion of multi-source remote sensing data by a deep learning model. *Front. Mar. Sci.* **2023**, *10*, 1140645. [CrossRef]
57. Minnett, P.J.; Alvera-Azcárate, A.; Chin, T.M.; Corlett, G.K.; Gentemann, C.L.; Karagali, I.; Li, X.; Marsouin, A.; Marullo, S.; Maturi, E.; et al. Half a century of satellite remote sensing of sea-surface temperature. *Remote Sens. Environ.* **2019**, *233*, 111366. [CrossRef]
58. Provost, C.; Garçon, V.; Falcon, L.M. Hydrographic conditions in the surface layers over the slope-open ocean transition area near the Brazil-Malvinas confluence during austral summer 1990. *Cont. Shelf Res.* **1996**, *16*, 215–235. [CrossRef]
59. Artana, C.; Provost, C.; Lellouche, J.M.; Rio, M.H.; Ferrari, R.; Sennéchael, N. The Malvinas Current at the Confluence with the Brazil Current: Inferences from 25 years of Mercator Ocean reanalysis. *J. Geophys. Res. Ocean.* **2019**, *124*, 7178–7200. [CrossRef]
60. Guerrero, R.A.; Acha, E.M.; Framiñan, M.B.; Lasta, C.A. Physical oceanography of the Río de la Plata estuary, Argentina. *Cont. Shelf Res.* **1997**, *17*, 727–742. [CrossRef]
61. Piola, A.R.; Matano, R.P.; Palma, E.D.; Möller, O.O., Jr.; Campos, E.J.D. The influence of the Plata River discharge on the western South Atlantic shelf. *Geophys. Res. Lett.* **2005**, *32*, L01603. [CrossRef]
62. Acha, E.M.; Mianzan, H.; Guerrero, R.; Carreto, J.; Giberto, D.; Montoya, N.; Carignan, M. An overview of physical and ecological processes in the Rio de la Plata Estuary. *Cont. Shelf Res.* **2008**, *28*, 1579–1588. [CrossRef]
63. Campos, E.J.D.; Piola, A.R.; Matano, R.P.; Miller, J.L. PLATA: A synoptic characterization of the southwest Atlantic shelf under influence of the Plata River and Patos Lagoon outflows. *Cont. Shelf Res.* **2008**, *28*, 1551–1555. [CrossRef]
64. Dogliotti, A.I.; Ruddick, K.; Guerrero, R. Seasonal and inter-annual turbidity variability in the Río de la Plata from 15 years of MODIS: El Niño dilution effect. *Estuar. Coast. Shelf Sci.* **2016**, *182*, 27–39. [CrossRef]
65. Borús, J.; Giacosa, J. Evaluación de Caudales Diarios Descargados Por Los Grandes Ríos Del Sistema Del Plata al Río de La Plata. In *Direccion y Alerta Hidrológico*; Instituto Nacional del Agua: Ezeiza, Argentina, 2014.
66. Burrage, D.; Wesson, J.; Martinez, C.; Pérez, T.; Möller, O., Jr.; Piola, A. Patos Lagoon outflow within the Río de la Plata plume using an airborne salinity mapper: Observing an embedded plume. *Cont. Shelf Res.* **2008**, *28*, 1625–1638. [CrossRef]

67. Campos, E.J.D.; Lorenzzetti, J.A.; Stevenson, M.R.; Stech, J.L.; de Souza, R.B. Penetration of waters from the Brazil–Malvinas Confluence region along the South American continental shelf up to 23°S. *An. Da Acad. Bras. De Ciências* **1996**, *68* (Suppl. 1), 49–58.
68. Campos, E.J.D.; Lentini, C.A.D.; Miller, J.L.; Piola, A.R. Interannual variability of the sea surface temperature in the South Brazil Bight. *Geophys. Res. Lett.* **1999**, *26*, 2061–2064. [CrossRef]
69. Palma, E.D.; Matano, R.P.; Piola, A.R. A numerical study of the Southwestern Atlantic Shelf circulation: Stratified ocean response to local and offshore forcing. *J. Geophys. Res. Ocean.* **2008**, *113*, C11010. [CrossRef]
70. García, N.O.; Vargas, W.M. The temporal climatic variability in the 'Río de la Plata' basin displayed by the river discharges. *Clim. Chang.* **1998**, *38*, 359–379. [CrossRef]
71. Framiñan, M.B.; Etala, M.P.; Acha, E.M.; Guerrero, R.A.; Lasta, C.A.; Brown, O.B. Physical characteristics and processes of the Río de la Plata Estuary. In *Estuaries of South America, Their Geomorphology and Dynamics*; Perillo, G.M.E., Piccolo, M.C., Pino-Quivira, M., Eds.; Springer: Berlin/Heidelberg, Germany, 1999; pp. 161–194.
72. Simionato, C.G.; Nuñez, M.N.; Engel, M. The salinity front of the Río de la Plata—A numerical case study for winter and summer conditions. *Geophys. Res. Lett.* **2001**, *28*, 2641–2644. [CrossRef]
73. Möller, O.O., Jr.; Piola, A.R.; Freitas, A.C.; Campos, E.J.D. The effects of river discharge and seasonal winds on the shelf off southeastern South America. *Cont. Shelf Res.* **2008**, *28*, 1607–1624. [CrossRef]
74. Moreira, D.; Simionato, C. The Río de la Plata estuary hydrology and circulation. *Meteorologica* **2019**, *44*, 1–30.
75. Lisboa, P.V.; Fernandes, E.H.; Sottolichio, A.; Huybrechts, N.; Bendo, A.R. Coastal plumes contribution to the suspended sediment transport in the Southwest Atlantic inner continental shelf. *J. Mar. Syst.* **2022**, *236*, 103796. [CrossRef]
76. Piola, A.R.; Palma, E.D.; Bianchi, A.A.; Castro, B.M.; Dottori, M.; Guerrero, R.A.; Marrari, M.; Matano, R.P.; Möller, O.O.; Saraceno, M. Physical oceanography of the SW Atlantic Shelf: A review. In *Plankton Ecology of the Southwestern Atlantic: From the Subtropical to the Subantarctic Realm*; Hoffmeyer, M.S., Sabatini, M.E., Brandini, F.P., Calliari, D.L., Santinelli, N.H., Eds.; Springer: Cham, Switzerland, 2018; pp. 37–56. [CrossRef]
77. Framiñan, M.B.; Brown, O.B. Study of the Río de la Plata turbidity front, Part 1: Spatial and temporal distribution. *Cont. Shelf Res.* **1996**, *16*, 1259–1282. [CrossRef]
78. Maciel, F.P.; Santoro, P.E.; Pedocchi, F. Spatio-temporal dynamics of the Río de la Plata turbidity front; combining remote sensing with in-situ measurements and numerical modeling. *Cont. Shelf Res.* **2021**, *213*, 104301. [CrossRef]
79. Matano, R.P.; Combes, V.; Piola, A.R.; Guerrero, R.; Palma, E.D.; Strub, P.T.; James, C.; Fenco, H.; Chao, Y.; Saraceno, M. The salinity signature of the cross-shelf exchanges in the Southwestern Atlantic Ocean: Numerical simulations. *J. Geophys. Res. Ocean.* **2014**, *119*, 7949–7968. [CrossRef]
80. Acha, E.M.; Mianzan, H.W.; Guerrero, R.A.; Favero, M.; Bava, J. Marine fronts at the continental shelves of austral South America: Physical and ecological processes. *J. Mar. Syst.* **2004**, *44*, 83–105. [CrossRef]
81. Brun, A.A.; Ramirez, N.; Pizarro, O.; Piola, A.R. The role of the Magellan Strait on the southwest South Atlantic shelf. *Estuar. Coast. Shelf Sci.* **2020**, *237*, 106661. [CrossRef]
82. Glorioso, P.D. Temperature distribution related to shelf-sea fronts on the Patagonian shelf. *Cont. Shelf Res.* **1987**, *7*, 27–34. [CrossRef]
83. Palma, E.D.; Matano, R.P.; Tonini, M.H.; Martos, P.; Combes, V. Dynamical analysis of the oceanic circulation in the Gulf of San Jorge, Argentina. *J. Mar. Syst.* **2020**, *203*, 103261. [CrossRef]
84. Combes, V.; Matano, R.P. The Patagonian shelf circulation: Drivers and variability. *Prog. Oceanogr.* **2018**, *167*, 24–43. [CrossRef]
85. Piola, A.R.; Campos, E.J.D.; Möller, O.O., Jr.; Charo, M.; Martinez, C. Subtropical shelf front off eastern South America. *J. Geophys. Res. Ocean.* **2000**, *105*, 6566–6578. [CrossRef]
86. Piola, A.R.; Möller, O.O., Jr.; Guerrero, R.A.; Campos, E.J.D. Variability of the subtropical shelf front off eastern South America: Winter 2003 and summer 2004. *Cont. Shelf Res.* **2008**, *28*, 1639–1648. [CrossRef]
87. Muelbert, J.H.; Acha, M.; Mianzan, H.; Guerrero, R.; Reta, R.; Braga, E.S.; Garcia, V.M.T.; Berasategui, A.; Gomez-Erache, M.; Ramírez, F. Biological, physical and chemical properties at the Subtropical Shelf Front Zone in the SW Atlantic Continental Shelf. *Cont. Shelf Res.* **2008**, *28*, 1662–1673. [CrossRef]
88. Palma, E.D.; Matano, R.P. A numerical study of the Magellan Plume. *J. Geophys. Res. Ocean.* **2012**, *117*, C05041. [CrossRef]
89. Guihou, K.; Piola, A.R.; Palma, E.D.; Chidichimo, M.P. Dynamical connections between large marine ecosystems of austral South America based on numerical simulations. *Ocean Sci.* **2020**, *16*, 271–290. [CrossRef]
90. Alsdorf, D.; Beighley, E.; Laraque, A.; Lee, H.; Tshimanga, R.; O'Loughlin, F.; Mahé, G.; Dinga, B.; Moukandi, G.; Spencer, R.G. Opportunities for hydrologic research in the Congo Basin. *Rev. Geophys.* **2016**, *54*, 378–409. [CrossRef]
91. Denamiel, C.; Budgell, W.P.; Toumi, R. The Congo River plume: Impact of the forcing on the far-field and near-field dynamics. *J. Geophys. Res. Ocean.* **2013**, *118*, 964–989. [CrossRef]
92. Vic, C.; Berger, H.; Tréguier, A.M.; Couvelard, X. Dynamics of an equatorial river plume: Theory and numerical experiments applied to the Congo plume case. *J. Phys. Oceanogr.* **2014**, *44*, 980–994. [CrossRef]
93. Tshimanga, R.M.; Moukandi N'kaya, G.D.; Alsdorf, D. (Eds.) *Congo Basin Hydrology, Climate, and Biogeochemistry: A Foundation for the Future*; American Geophysical Union, Geophysical Monograph Series; Wiley: Hoboken, NJ, USA, 2022; Volume 269, 592p.
94. Sorí, R.; Nieto, R.; Vicente-Serrano, S.M.; Drumond, A.; Gimeno, L. A Lagrangian perspective of the hydrological cycle in the Congo River basin. *Earth Syst. Dyn.* **2017**, *8*, 653–675. [CrossRef]

95. Munzimi, Y.A.; Hansen, M.C.; Asante, K.O. Estimating daily streamflow in the Congo Basin using satellite-derived data and a semi-distributed hydrological model. *Hydrol. Sci. J.* **2019**, *64*, 1472–1487. [CrossRef]
96. Phillipson, L.; Toumi, R. Assimilation of satellite salinity for modelling the Congo River plume. *Remote Sens.* **2019**, *12*, 11. [CrossRef]
97. Laraque, A.; Moukandi N'kaya, G.D.; Orange, D.; Tshimanga, R.; Tshitenge, J.M.; Mahé, G.; Nguimalet, C.R.; Trigg, M.A.; Yepez, S.; Gulemvuga, G. Recent budget of hydroclimatology and hydrosedimentology of the Congo River in Central Africa. *Water* **2020**, *12*, 2613. [CrossRef]
98. Jarugula, S.; McPhaden, M.J. Indian Ocean Dipole affects eastern tropical Atlantic salinity through Congo River Basin hydrology. *Commun. Earth Environ.* **2023**, *4*, 366. [CrossRef]
99. Wongchuig, S.; Kitambo, B.; Papa, F.; Paris, A.; Fleischmann, A.S.; Gal, L.; Boucharel, J.; Paiva, R.; Oliveira, R.J.; Tshimanga, R.M.; et al. Improved modeling of Congo's hydrology for floods and droughts analysis and ENSO teleconnections. *J. Hydrol. Reg. Stud.* **2023**, *50*, 101563. [CrossRef]
100. Shannon, L.V.; Agenbag, J.J.; Buys, M.E.L. Large- and mesoscale features of the Angola-Benguela front. *S. Afr. J. Mar. Sci.* **1987**, *5*, 11–34. [CrossRef]
101. Lass, H.U.; Schmidt, M.; Mohrholz, V.; Nausch, G. Hydrographic and current measurements in the area of the Angola–Benguela front. *J. Phys. Oceanogr.* **2000**, *30*, 2589–2609. [CrossRef]
102. Mohrholz, V.; Schmidt, M.; Lutjeharms, J.R.E.; John, H.C. Space–time behaviour of the Angola–Benguela Frontal Zone during the Benguela Niño of April 1999. *Int. J. Remote Sens.* **2004**, *25*, 1337–1340. [CrossRef]
103. Vizy, E.K.; Cook, K.H.; Sun, X. Decadal change of the South Atlantic Ocean Angola-Benguela frontal zone since 1980. *Clim. Dyn.* **2018**, *51*, 3251–3273. [CrossRef]
104. Andrews, W.R.H.; Hutchings, L. Upwelling in the southern Benguela Current. *Prog. Oceanogr.* **1980**, *9*, 1–81. [CrossRef]
105. Hutchings, L.; Van der Lingen, C.D.; Shannon, L.J.; Crawford, R.J.M.; Verheye, H.M.S.; Bartholomae, C.H.; Van der Plas, A.K.; Louw, D.; Kreiner, A.; Ostrowski, M.; et al. The Benguela Current: An ecosystem of four components. *Prog. Oceanogr.* **2009**, *83*, 15–32. [CrossRef]
106. Hutchings, L.; Armstrong, B.A.; Mitchell-Innes, D.A. The frontal zone in the southern Benguela Current. In *Marine Interfaces Eco-Hydrodynamics, Proceedings of the 17th International Liege Colloquium on Ocean Hydrodynamics, Liege, Belgium, 13–17 May 1985*; Nihoul, J.C.J., Ed.; Elsevier Oceanography Series; Elsevier: Amsterdam, The Netherlands, 1986; Volume 42, pp. 67–94. [CrossRef]
107. Armstrong, D.A.; Mitchell-Innes, B.A.; Verheye-Dua, F.; Waldron, H.; Hutchings, L. Physical and biological features across an upwelling front in the southern Benguela. *S. Afr. J. Mar. Sci.* **1987**, *5*, 171–190. [CrossRef]
108. Belkin, I.M.; Cornillon, P.C.; Sherman, K. Fronts in Large Marine Ecosystems. *Prog. Oceanogr.* **2009**, *81*, 223–236. [CrossRef]
109. Duncombe Rae, C.M. A demonstration of the hydrographic partition of the Benguela upwelling ecosystem at 26°40′S. *Afr. J. Mar. Sci.* **2005**, *27*, 617–628. [CrossRef]
110. Muller, A.A.; Mohrholz, V.; Schmidt, M. The circulation dynamics associated with a northern Benguela upwelling filament during October 2010. *Cont. Shelf Res.* **2013**, *63*, 59–68. [CrossRef]
111. Belkin, I.M.; Gordon, A.L. Southern Ocean fronts from the Greenwich meridian to Tasmania. *J. Geophys. Res. Ocean.* **1996**, *101*, 3675–3696. [CrossRef]
112. Smythe-Wright, D.; Chapman, P.; Duncombe Rae, C.; Shannon, L.V.; Boswell, S.M. Characteristics of the South Atlantic subtropical frontal zone between 15°W and 5°E. *Deep-Sea Res. Part I* **1998**, *45*, 167–192. [CrossRef]
113. Juliano, M.F.; Alves, M.L. The Atlantic subtropical front/current systems of Azores and St. Helena. *J. Phys. Oceanogr.* **2007**, *37*, 2573–2598. [CrossRef]
114. Vianna, M.L.; Menezes, V.V. Double-celled subtropical gyre in the South Atlantic Ocean: Means, trends, and interannual changes. *J. Geophys. Res. Ocean.* **2011**, *116*, C03024. [CrossRef]
115. Funke, M. On the Subtropical Front in the South Atlantic Ocean. Master's Thesis, University of Cape Town, Cape Town, South Africa, 2009; 82p. Available online: http://hdl.handle.net/11427/6473 (accessed on 24 April 2024).
116. Peterson, R.G.; Stramma, L. Upper-level circulation in the South Atlantic Ocean. *Prog. Oceanogr.* **1991**, *26*, 1–73. [CrossRef]
117. Kerr, Y.H.; Waldteufel, P.; Wigneron, J.P.; Delwart, S.; Cabot, F.; Boutin, J.; Escorihuela, M.J.; Font, J.; Reul, N.; Gruhier, C.; et al. The SMOS mission: New tool for monitoring key elements of the global water cycle. *Proc. IEEE* **2010**, *98*, 666–687. [CrossRef]
118. Olmedo, E.; González-Haro, C.; Hoareau, N.; Umbert, M.; González-Gambau, V.; Martínez, J.; Gabarró, C.; Turiel, A. Nine years of SMOS sea surface salinity global maps at the Barcelona Expert Center. *Earth Syst. Sci. Data* **2021**, *13*, 857–888. [CrossRef]
119. Belkin, I.M.; O'Reilly, J.E. An algorithm for oceanic front detection in chlorophyll and SST satellite imagery. *J. Mar. Syst.* **2009**, *78*, 317–326. [CrossRef]
120. Belkin, I.M. Remote sensing of ocean fronts in marine ecology and fisheries. *Remote Sens.* **2021**, *13*, 883. [CrossRef]
121. Gallagher, N.C.; Wise, G.L. A theoretical analysis of the properties of median filters. *IEEE Trans. Acoust. Speech Signal Process.* **1981**, *29*, 1136–1141. [CrossRef]
122. Irons, J.R.; Petersen, G.W. Texture transforms of remote sensing data. *Remote Sens. Environ.* **1981**, *11*, 359–370. [CrossRef]
123. Curran-Everett, D. Explorations in statistics: The log transformation. *Adv. Physiol. Educ.* **2018**, *42*, 343–347. [CrossRef]
124. Gonzalez, R.C.; Woods, R.E. *Digital Image Processing*, 4th ed.; Pearson: London, UK, 2018.
125. Gonzalez, R.C.; Woods, R.E.; Eddins, S.L. *Digital Image Processing Using MATLAB®*, 3rd ed.; Gatesmark Publishing: Knoxville, TN, USA, 2020.

126. Campbell, J.W. The lognormal distribution as a model for bio-optical variability in the sea. *J. Geophys. Res.* **1995**, *100*, 13237–13254. [CrossRef]
127. Gregg, W.W.; Casey, N.W. Global and regional evaluation of the SeaWiFS chlorophyll data set. *Remote Sens. Environ.* **2004**, *93*, 463–479. [CrossRef]
128. Werdell, P.J.; McKinna, L.I.W.; Boss, E.; Ackleson, S.G.; Craig, S.E.; Gregg, W.W.; Lee, Z.P.; Maritorena, S.; Roesler, C.S.; Rousseaux, C.S.; et al. An overview of approaches and challenges for retrieving marine inherent optical properties from ocean color remote sensing. *Prog. Oceanogr.* **2018**, *160*, 186–212. [CrossRef]
129. Zhang, F.; Li, X.F.; Hu, J.Y.; Sun, Z.Y.; Zhu, J.; Chen, Z.Z. Summertime sea surface temperature and salinity fronts in the southern Taiwan Strait. *Int. J. Remote Sens.* **2014**, *35*, 4452–4466. [CrossRef]
130. Stramma, L.; Peterson, R.G. The South Atlantic Current. *J. Phys. Oceanogr.* **1990**, *20*, 846–859. [CrossRef]
131. Belkin, I.M. Frontal structure of the South Atlantic. In *Pelagic Ecosystems of the Southern Ocean*; Voronina, N.M., Ed.; Nauka: Moscow, Russia, 1993; pp. 40–53. (In Russian)
132. Kolodziejczyk, N.; Hernandez, O.; Boutin, J.; Reverdin, G. SMOS salinity in the subtropical North Atlantic salinity maximum: 2. Two-dimensional horizontal thermohaline variability. *J. Geophys. Res. Ocean.* **2015**, *120*, 972–987. [CrossRef]
133. Gordon, A.L.; Giulivi, C.F.; Busecke, J.; Bingham, F.M. Differences among subtropical surface salinity patterns. *Oceanography* **2015**, *28*, 32–39. [CrossRef]
134. Peterson, R.G.; Whitworth, T., III. The Subantarctic and Polar Fronts in relation to deep water masses through the southwestern Atlantic. *J. Geophys. Res. Ocean.* **1989**, *94*, 10817–10838. [CrossRef]
135. Aubriot, L.; Zabaleta, B.; Bordet, F.; Sienra, D.; Risso, J.; Achkar, M.; Somma, A. Assessing the origin of a massive cyanobacterial bloom in the Río de la Plata (2019): Towards an early warning system. *Water Res.* **2020**, *181*, 115944. [CrossRef] [PubMed]
136. Kruk, C.; Martínez, A.; de la Escalera, G.M.; Trinchin, R.; Manta, G.; Segura, A.M.; Piccini, C.; Brena, B.; Yannicelli, B.; Fabiano, G.; et al. Rapid freshwater discharge on the coastal ocean as a mean of long distance spreading of an unprecedented toxic cyanobacteria bloom. *Sci. Total Environ.* **2021**, *754*, 142362. [CrossRef]
137. Piola, A.R.; Romero, S.I. Space-time variability of the Plata River Plume. *Gayana (Concepción)* **2004**, *68*, 482–486. [CrossRef]
138. Marta-Almeida, M.; Dalbosco, A.; Franco, D.; Ruiz-Villarreal, M. Dynamics of river plumes in the South Brazilian Bight and South Brazil. *Ocean Dyn.* **2021**, *71*, 59–80. [CrossRef]
139. Dávila, P.M.; Figueroa, D.; Müller, M. Freshwater input into the coastal ocean and its relation with the salinity distribution off austral Chile (35–55°S). *Cont. Shelf Res.* **2002**, *22*, 521–534. [CrossRef]
140. Ekau, W.; Verheye, H.M. Influence of oceanographic fronts and low oxygen on the distribution of ichthyoplankton in the Benguela and southern Angola currents. *Afr. J. Mar. Sci.* **2005**, *27*, 629–639. [CrossRef]
141. Gammelsrød, T.; Bartholomae, C.H.; Boyer, D.C.; Filipe, V.L.L.; O'Toole, M.J. Intrusion of warm surface water along the Angolan-Namibian coast in February–March 1995: The 1995 Benguela Nino. *S. Afr. J. Mar. Sci.* **1998**, *19*, 41–56. [CrossRef]
142. von Bodungen, B.; John, H.C.; Lutjeharms, J.R.E.; Mohrholz, V.; Veitch, J. Hydrographic and biological patterns across the Angola–Benguela Frontal Zone under undisturbed conditions. *J. Mar. Syst.* **2008**, *74*, 189–215. [CrossRef]
143. Aubone, N.; Palma, E.D.; Piola, A.R. The surface salinity maximum of the South Atlantic. *Prog. Oceanogr.* **2021**, *191*, 102499. [CrossRef]